Development of an Application for Assessing Air-Breathing Electric Propulsion Feasibility in Very-Low Earth Orbits

Raquel Fecha Coutinho

Dissertação para obtenção do Grau de Mestre em

Engenharia Aeronáutica

(Mestrado integrado)

Orientador: Prof. Doutor André Resende Rodrigues da Silva
Co-orientador: Doutor Eng. Jorge André Almeida Barreto
Co-orientador: Eng. Diogo Portugal Abranches

outubro de 2023

Declaração de Integridade

Eu, Raquel Fecha Coutinho, que abaixo assino, estudante com o número de inscrição 41 821 de Engenharia Aeronáutica da Faculdade de Engenharia, declaro ter desenvolvido o presente trabalho e elaborado o presente texto em total consonância com o **Código de Integridades da Universidade da Beira Interior**.

Mais concretamente afirmo não ter incorrido em qualquer das variedades de Fraude Académica, e que aqui declaro conhecer, que em particular atendi à exigida referenciação de frases, extratos, imagens e outras formas de trabalho intelectual, e assumindo assim na íntegra as responsabilidades da autoria.

Universidade da Beira Interior, Covilhã 06/10/2023

Assinado por: **Raquel Fecha Coutinho**
Num. de Identificação: 13850299
Data: 2023.10.06 11:31:58+01'00'

CHAVE MÓVEL

Dedicatória

Dedico esta dissertação à minha família e amigos.

Agradecimentos

Em primeiro lugar, expresso a minha gratidão à Omnidea pela oportunidade de desenvolver esta dissertação com o seu apoio. Gostaria de destacar os engenheiros Jorge Barreto e Diogo Abranches pela sua orientação excecional, compartilhamento de conhecimento e simpatia ao longo deste trabalho. Não posso deixar de mencionar o ambiente de trabalho incrível proporcionado por toda a equipa, o que tornou estes meses de pesquisa ainda mais enriquecedores.

Agradeço ao Prof. Doutor André Silva pela disponibilidade e orientação. Assim como, aos experientes Francesco Romano e Yaroslav Mashtakov pela ajuda que contribuiu significativamente para este projeto.

Por fim, dedico um agradecimento especial aos meus pais e irmãos, cujo apoio e amor tornaram possível a concretização desta etapa. Aos amigos que me acompanharam ao longo deste percurso académico, tornando minha passagem pela Covilhã inesquecível.

Resumo

Órbitas terrestres muito baixas oferecem inúmeras vantagens para as missões de observação terrestre como, por exemplo, melhor resolução e redução do custo. No entanto, baixar a altitude operacional dos satélites introduz certos desafios, tais como: maior densidade atmosférica e, consequentemente, maior resistência atmosférica e energia requerida. A propulsão eléctrica convencional tem dificuldade em manter estas missões em órbitas muito baixas durante períodos prolongados devido ao arrasto atmosférico significativo que esgota o propelente a bordo. Por consequência, a tecnologia *air-breathing electric propulsion* (ABEP) tornou-se promissora uma vez que utiliza o atmosfera residual circundante como propelente para a geração de tração. No entanto, o desempenho dos propulsores eléctricos piora devido à necessidade de colectar a atmosfera em regime molecular através de um sistema de admissão. Além disso, as espécies atmosféricas têm um desempenho inferior em comparação com propelentes típicos como o xénon.

Esta tese tem como objetivo identificar os requisitos para manter a altitude de um veículo espacial em órbitas muito baixas e avaliar a viabilidade da utilização da tecnologia ABEP para este fim. Para tal, foi desenvolvida uma aplicação em MATLAB® para caracterizar o ambiente orbital e calcular o desempenho necessário para operar numa missão helio-síncrona especificada pelo utilizador. A missão GOCE, que orbitou a altitudes muito baixas, foi reproduzida pela aplicação e os seus resultados foram validados comparando-os com os dados de voo reportados. Além disso, os resultados da simulação forneceram informações valiosas sobre a viabilidade da incorporação deste tipo de propulsores eléctricos em missões semelhantes à GOCE.

Palavras-chave

Air-breathing electric propulsion;Órbitas terrestres muito baixas;MATLAB®;Estudo de viabilidade

Abstract

Very-low Earth orbits offer numerous advantages for Earth observation missions, including improved resolution and reduced cost. However, lowering spacecraft orbits introduces certain operational challenges such as: higher atmospheric density and, consequently, increased atmospheric drag and power demand. Conventional electrical propulsion struggles to sustain VLEO missions for extended periods due to the substantial drag that depletes onboard propellant. Therefore, air-breathing electric propulsion (ABEP) has emerged as a promising technology by utilizing the surrounding air for thrust generation and reducing reliance on onboard propellants. However, the performance of electric thrusters worsens due to the need to collect the atmosphere in free-molecular regime through an intake system. Additionally, atmospheric species have inferior performance in thrust generation compared to typical propellants like xenon.

This thesis aims to identify the requirements for sustaining a spacecraft's orbit in VLEO and assess the feasibility of utilizing state-of-the-art ABEP technology for this purpose. To achieve this, a MATLAB® application was developed to characterize the very-low environment and compute the required performance to operate in a sun-synchronous mission specified by the user. GOCE mission that orbited in very-low altitudes was replicated by the app and its outputs were validated by comparing them to the reported flight data. Moreover, the simulation outcomes provided valuable insights into the feasibility of incorporating air-breathing electric thrusters in missions similar to GOCE's.

Keywords

Air-breathing electric propulsion;Very-low Earth orbits;MATLAB®;Feasibility study

Contents

List of Figures

List of Tables

Nomenclature

J_2	Zonal harmonic coefficient	-
$F10.7$	Solar flux emitted in a wavelength of 10.7 cm	sfu
Ap	Geomagnetic planetary index	-
AO	Anomalous oxygen	-
F_D	Drag force	N
ρ	Atmospheric density	$\frac{kg}{m^3}$
C_D	Drag coefficient	-
A_f	Frontal area	m^2
v	Orbital velocity	$\frac{m}{s}$
Kn	Knudsen number	-
λ	Mean free path	m
l_{ref}	Characteristic length	m
α_E	Accommodation coefficient	-
E_i	Energy of the incoming particles	J
E_r	Energy of the reflected particles	J
E_w	Energy of completely accommodated particles	J
I_{sp}	Specific impulse	s
T	Thrust	N
η_t	Total efficiency	-
P_{in}	Power input	W
g_0	Gravitational acceleration constant	$\frac{m}{s^2}$
v_e	Exhaust velocity	$\frac{m}{s}$
$\dot{m}$	Mass flow rate	$\frac{kg}{s}$
$\dot{v}$	Volume flow rate	sccm
η_c	Collection efficiency	-
β	Compression factor	-
$\vec{r}$	Spacecraft position vector	(m, m, m) or (°, °, m)
μ	Earth's gravitational parameter	$\frac{m^3}{s^2}$
a	Semi-major axis	m
a_e	Equatorial radius of the Earth	m
i	Inclination	°

e	Eccentricity	-
Ω	Right ascension of the ascending node	$^\circ$
ω	Argument of the perigee	$^\circ$
υ	True anomaly	$^\circ$
T_o	Period	s
$\vec{a_p}$	Perturbation acceleration	$\frac{m}{s^2}$
p	Orbital parameter	m
n	Mean motion	s^{-1}
h	Ellipsoidal altitude	m
ϕ	Geodetic latitude	$^\circ$
λ	Geodetic longitude	$^\circ$

List of Abbreviations

ABEP	Air-Breathing Electric Propulsion
ABET	Air-Breathing Electric Thrusters
ABIE	Air-Breathing Ion Engine
AETHER	Air-Breathing Electric THrustER
ECEF	Earth-Centered Earth-Fixed
ECR	Electron Cyclotron Ressonance
EO	Earth Observation
EP	Electric Propulsion
ESA	European Space Agency
FMF	Free Molecular Flow
GIT	Gridded Ion Thrusters
GOCE	Gravity Field and Steady-State Ocean Circulation Explorer
GSI	Gas-Surface Interaction
HET	Hall Effect Thrusters
HPT	Helicon Plasma Thruster
IPT	Inductive Plasma Thruster
IRS	Institute Of Space Sytems
ITRF	International Terrestrial Reference Frame
JAXA	Japan Aerospace Exploration Agency
NRLMSISE-00	Naval Research Laboratory Mass Spectrometer and Incoherent Scatter Radar Exosphere Model
MABHET	Martian Air-Breathing Hall-Effect Thruster
ODE	Ordinary Differential Equations
RAAN	Right Ascension Of The Ascending Node
RF	Radiofrequency
RIT	Radiofrequency Ion Thrusters
SA	Solar Arrays
SLATS	Super Low Altitude Test Satellite
SoA	State-Of-The-Art
SOAR	Satellite For Orbital Aerodynamics Research

SSO	Sun-Synchronous Orbits
VLEO	Very-Low Earth Orbit
WGS84	World Geodetic System 1984

Chapter 1

Introduction

Very-low Earth orbits (VLEO), commonly classified as orbits below $450\,\mathrm{km}$, offer a number of benefits that can significantly improve the design and performance of satellites, particularly for remote sensing and Earth Observation (EO) applications. Reducing orbital altitude below those conventionally used enables [1]:

- Optical payload to increase in resolution or reduce aperture size resulting in either improved performance or smaller size and mass.
- Radiometric performance improvement by reducing the distance to the target, allowing improved signal-to-noise ratio and reduced latency. Radar and communications applications also benefit from reduced altitude leading to improved link budgets, reduction in power, and smaller antenna areas.
- No deorbit mechanisms are required as an unpropelled spacecraft naturally deorbits due to atmospheric drag within a few years or even weeks depending on both altitude and configuration [2].
- Lower risk of collision with space debris as they naturally undergo deorbiting. VLEO are resilient to orbital debris built-ups, which is a prevalent problem at higher altitudes.
- Reduced launch costs as the same performance can be achieved with a smaller payload.

However, operating in very-low orbits presents new challenges mainly related to the residual atmosphere. These challenges include increased atmospheric density, resulting in higher experienced atmospheric drag by spacecraft. Additionally, there is a significant presence of atomic oxygen which cause erosion and degradation of spacecraft surfaces. As a result, this region remains not widely exploited as state-of-the-art (SoA) technology has not been yet sufficiently developed for orbit maintenance for a long period of time. As shown in Figure 1.1, the number of satellites operating at high altitude orbits is large, but there are almost no satellites working in VLEO.

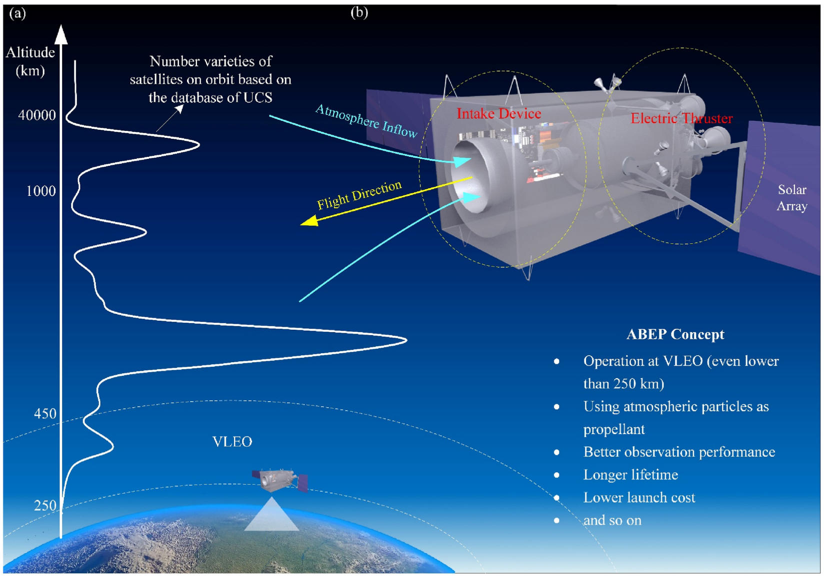

Figure 1.1: (a) Number varieties of satellites in orbit. (b) Air-breathing electric propulsion concept [3].

Traditional chemical and electric space propulsion systems rely on on-board propellant that is unable to maintain a spacecraft in orbit for extended periods due to the substantial drag experienced in near-Earth orbits. Once the system runs out of propellant, it ceases to counteract the drag force, leading to a decrease in acceleration. Consequently, the spacecraft initiates its orbital decay, eventually leading to re-entry into the atmosphere and its ultimate demise.

The emergent technology Air-Breathing Electric Propulsion (ABEP) aims to address these barriers to enable the sustainable operation of spacecraft in VLEO. ABEP is an alternative approach by utilizing residual atmospheric particles to generate thrust, thereby counteracting the effects of atmospheric drag without carrying conventional propellant on-board. This technology is currently under development with numerous ongoing studies. Omnidea is a Portuguese aerospace company that is actively conducting research in this field and proposed the development of the present thesis within its activities.

The objective of this thesis is to create an application capable of calculating the required propulsive performance for maintaining a spacecraft in VLEO utilizing an ABEP system. The user is prompted to input key mission parameters such as orbital altitude, mission duration, and spacecraft frontal area. Based on the provided mission details, the application then computes the essential propulsive parameters needed to effectively counteract drag throughout the mission. The primary outputs encompass the required thrust profile, electric power profile, and the specific impulse, along with other pertinent atmospheric and orbital parameters. The tool is developed using MATLAB® and the study is specifically focused on sun-synchronous orbits that demonstrate significant potential for enhancing air-breathing missions.

The results generated by the app are validated by comparing simulated data with actual flight data. To achieve this validation, GOCE mission is simulated due to its operation at very-low altitudes. Lastly, a mission with a spacecraft geometry and orbit similar to that of GOCE is analyzed within the feasible altitude range for air-breathing electric propulsion to evaluate the possibility of using this technology to counteract drag throughout the mission.

The outcomes generated by this app will provide insights into the feasibility of employing air-breathing technology in very-low missions and highlight the need for additional development to enhance its viability.

1.1 Outline

To enhance the understanding of the subject, this thesis is structured in chapters as follows:

- **Chapter 1: Introduction**

  The introduction provides an overview of the benefits associated with very-low orbits for EO, remote sensing, communications, and radar missions, emphasizing the significance of developing ABEP technology as a potential solution to enable the exploitation of this region. The objective of this thesis is also outlined as the importance of its findings.

- **Chapter 2: The very-low Earth orbit environment**

  In this chapter, a comprehensive characterization of the very-low orbit environment is conducted to gain insights into the challenges that ABEP technology must overcome.

- **Chapter 3: Air-breathing electric propulsion**

  In this chapter, a literature review of ABEP is carried out. The chapter begins by examining the fundamentals of traditional electric propulsion. Subsequently, the concept of an air-breathing engine is introduced, and the challenges that traditional thrusters encounter when operating in this mode are outlined. Finally, the chapter concludes with a comprehensive review of the SoA of ABEP, providing an overview of the latest advancements and developments in the field.

- **Chapter 4: App development**

  In this chapter, the process involved in the development of the application is explained. The flowchart is analyzed in detail as pieces of code are presented. Moreover, the GOCE mission is simulated and the obtained results are compared to the existing reported flight data to validate the application.

- **Chapter 5: Case-study**

  In this chapter, the feasibility of employing an air-breathing electric engine on a mission similar to GOCE's is examined using the developed app. For this analysis, a spacecraft geometry and an orbit similar to GOCE's are selected, and the operational altitude is chosen based on the feasible range of altitudes for air-breathing technology.

- **Chapter 6: Conclusion**

  The final chapter serves as a comprehensive summary of the conclusions drawn from the preceding chapters concerning the viability of spacecraft operation in VLEO utilizing an ABEP system. Additionally, this chapter outlines potential areas for further research and development.

Chapter 2

The very-low Earth orbit environment

Very-low Earth orbits are usually defined between $100\,\mathrm{km}$ (Kárman line) and $450\,\mathrm{km}$ of altitude. The interaction between the spacecraft and the atmosphere becomes more pronounced as the orbital altitude decreases due to the increase in atmospheric density. Therefore, aerodynamic forces and torques cannot be neglected. Aerodynamic torques will not be analyzed as the primary focus of the thesis is drag compensation and not orbit control. Figure 2.1 illustrates the relative significance of various perturbations in low Earth orbit.

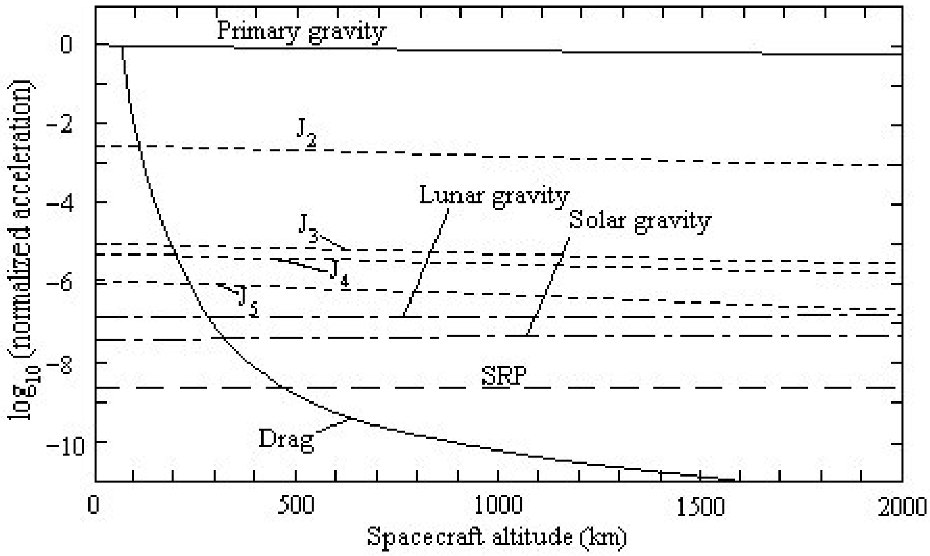

Figure 2.1: Significance of various disturbing accelerations on LEO [4].

The main sources of disturbing accelerations in VLEO are primary gravity, atmospheric drag, and the Earth's oblateness represented by the J_2 coefficient. Notably, as the orbital altitude decreases, the atmospheric drag increases significantly.

As previously mentioned, remote sensing activities would greatly benefit from very-low altitudes. However, such activities are commonly not operated in this region due to the environmental challenges it poses. This is mainly due to the presence of the residual atmosphere that leads to a large amount of on-board propellant required to compensate for drag force and stay in orbit. In addition, the considerable prevalence of atomic oxygen contributes to spacecraft erosion [2].

In this chapter, a detailed characterization of the very-low environment is undertaken to identify the specific requirements that an ABEP system must fulfill in order to enable successful orbital operations in this region.

2.1 Atmospheric composition

VLEO is indeed a dynamic environment, in which its composition undergoes spatial and temporal variations as a function of altitude, solar and geomagnetic activities (given by F10.7 and Ap parameters), geographic position (e.g., latitude and longitude), day-night cycles, and solar zenith angle [2]. The effect of altitude on atmospheric composition for a given day and geographic location is represented in Figure 2.2.

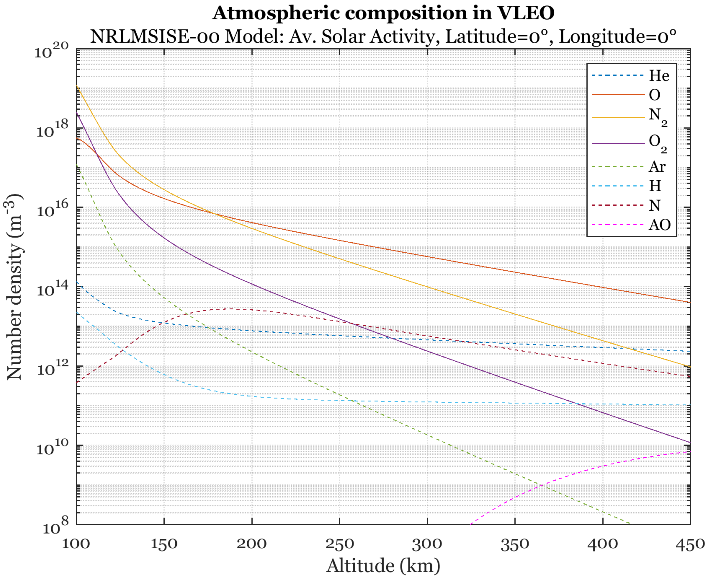

Figure 2.2: Atmospheric composition in VLEO.

The atmospheric density decreases with altitude due to the effect of Earth's gravity. The predominant species encountered in VLEO are molecular nitrogen (N_2), atomic oxygen (O), and molecular oxygen (O_2). Note that atomic oxygen becomes increasingly prevalent compared to O_2 at $\approx 110\,\mathrm{km}$ and the most abundant species at $\approx 200\,\mathrm{km}$ of altitude.

Being one of the main atmospheric constituents and highly reactive, atomic oxygen can damage materials and adsorbs to spacecraft surfaces causing erosion and affecting aerodynamics. Thus, materials resistant to atomic oxygen must be selected in order to maintain optimal performance and avoid degradation [4].

Also, atmospheric density largely depends on solar and geomagnetic activities [5]. Particular attention must be taken concerning solar activity that cycles every 11 years as depicted in Figure 2.3a. Geomagnetic activity is depicted in Figure 2.3b.

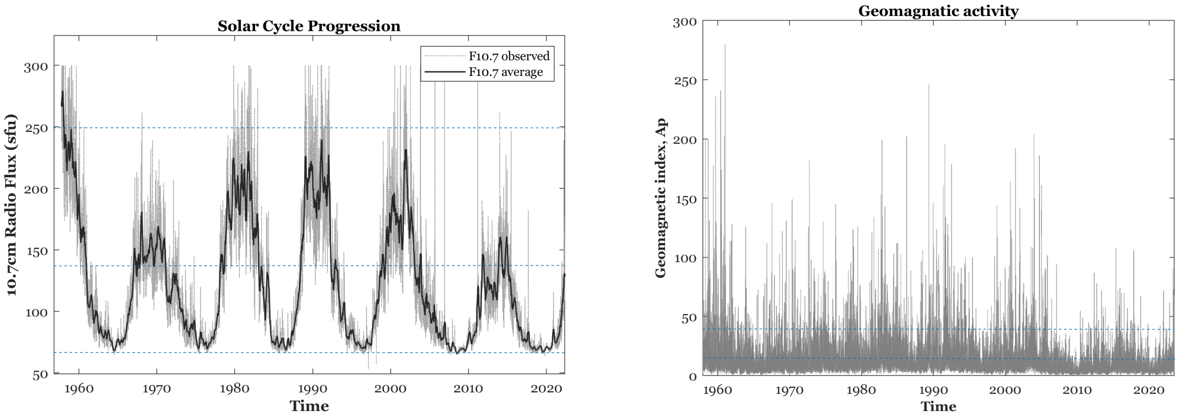

(a) (b)

Figure 2.3: Space-weather data from CelesTrak® [6].

$F10.7$ and Ap are two indices responsible for measuring solar radiation and geomagnetic activity levels. $F10.7$ index measures the solar flux emitted at a wavelength of $10.7\,\mathrm{cm}$ ($2800\,\mathrm{MHz}$) which is a suitable proxy for solar extreme ultraviolet radiation. In turn, the geomagnetic planetary index Ap measures the general level of geomagnetic activity on Earth for a given day. These parameters are commonly used by models because they are available for the longest period of time [7].

Figure 2.4a and 2.4b illustrates the effect of the solar and geomagnetic activities on atmospheric density and temperature, respectively. The values considered for minimum, average, and maximum activity are based on recorded events in Figures 2.3a and 2.3b.

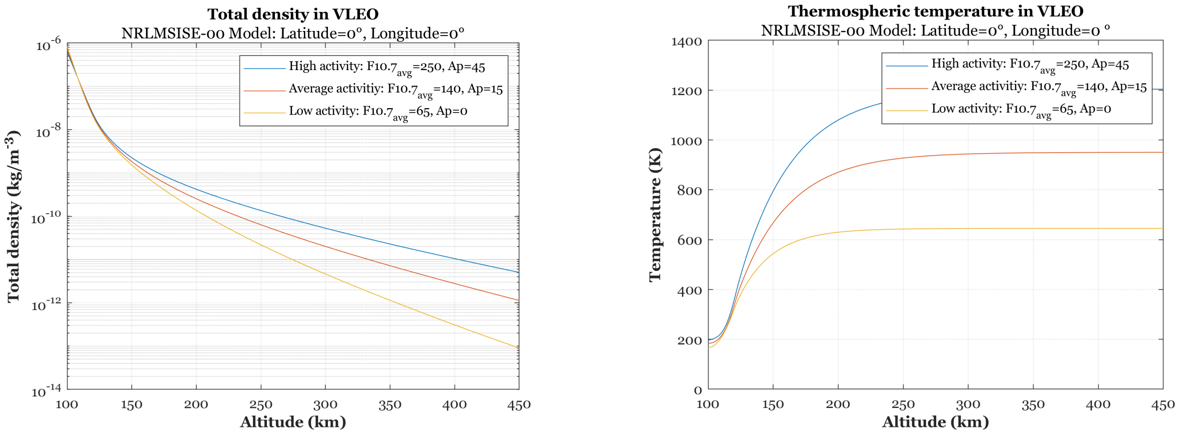

(a) (b)

Figure 2.4: Effect of solar and geomagnetic activities on (a) atmospheric density (b) atmospheric temperature.

The effect of solar activity weakens as altitude decreases, i.e., variations are milder for the lower region of VLEO. In general, higher solar activity leads to an increment in density and temperature for a given altitude. This change occurs due to the significant heating and consequent atmospheric expansion during high solar activity [8]. The thermosphere absorbs the ultraviolet energy resulting in a rapid temperature increase at its lower region while reaching a limit (exospheric temperature) at its upper region. The exospheric temperature is reached due to the infrequency of intermolecular collisions that occur as a result of the very low density [9].

Additionally, the solar exposure (illuminated or eclipsed side of the Earth) and the geographic position also influence the atmospheric density. This means that atmospheric properties are intrinsic to spacecraft operation and trajectory.

2.2 Drag

As previously mentioned, the increasing air density defines the environment of low altitudes. Drag force results from the interchange of momentum between the residual atmospheric particles and the surface of the spacecraft while colliding. As a result, the spacecraft's orbital energy gradually decreases limiting its lifetime. The magnitude of the drag effect depends on spacecraft geometry, attitude, surface properties, and orbital medium. The drag force F_D can be calculated as follows [9]:

$$F_D = \frac{1}{2}\rho C_D A_f v^2 \quad (2.1)$$

where ρ is the atmospheric density, C_D is the drag coefficient, A_f is the spacecraft frontal area and v is the orbital velocity relative to the thermosphere. The velocity of the spacecraft in VLEO is so high that the investigation considers the motion of the spacecraft traveling at high speeds through a gas at rest [10].

A good estimation of this force is difficult due to the large uncertainties associated with: atmospheric density, drag coefficient, and velocity of the body with respect to the thermosphere. The dynamic nature of the thermosphere turns the spacecraft's relative velocity (due to thermospheric winds) and atmospheric properties hard to predict. Also, Equation 2.1 neglects the significant contribution of the parallel surfaces for drag, as a simplification [11].

The orbiting medium can be classified by the Knudsen number (Kn) as continuous, transitional, or free molecular flow (FMF) in order of ascending altitude. Kn is a dimensionless number defined as [9]:

$$\mathrm{Kn} = \frac{\lambda}{l_{\mathrm{ref}}} \quad (2.2)$$

where λ is the mean free path of particles in motion (i.e., the mean distance between consecutive collisions) and l_{ref} is the characteristic length of the spacecraft.

A continuum flow regime in which particle-particle collisions play a dominant role in gas dynamics is classified by a Kn ≤ 0.01. In this scenario, the spacecraft's length greatly surpasses the mean free path of particles within the gas medium. A Kn ≥ 10 indicates the flow is FMF, where particle-wall collisions are dominant over particle-particle collisions. Continuum flows should be analyzed using the Navier-Stokes equations while FMF should apply the collisionless Boltzmann equation [9]. Flows in which Kn lies between these numbers are considered transitional where particle-particle and particle-wall collisions are equally relevant.

Bellow approximately $85\,\text{km}$ of altitude, the flow regime is classified as a continuum while above approximately $130\,\text{km}$ is classified as FMF [12]. The criteria for FMF are generally satisfied in VLEO, where λ is significantly greater than the l_{ref} of the body immersed in the flow and collisions between molecules are extremely rare.

It is worth noting that solar activity also has an influence on the flow regime. During periods of high solar activity, the atmospheric density at a given altitude increases, leading to a decrease in the Knudsen number [9].

According to the flow regime present at VLEO, the forces imparted on the body are calculated from the collision momentum transfer from the particle to the surface. The physical theory behind these collisions is captured in the Gas-Surface Interaction (GSI) models. A number of GSI models have been developed over the years assuming different assumptions about the particle-surface interactions and the re-emission characteristics. The model's accuracy depends on the undertaken assumptions such as environmental conditions and the surface materials. Most models rely on energy accommodation coefficients α_E which relate the extent of energy transfer from gas molecules to the surface and range from 0 to 1. This parameter is given by [9]:

$$\alpha_E = \frac{E_i - E_r}{E_i - E_w} \tag{2.3}$$

where E_i and E_r are the kinetic energies carried by the incident and the scattered fluxes, while E_w is the energy flux that would be carried away if all the molecules were reemitted diffusely in thermal equilibrium with the surface, such that they have the same temperature as the surface. When a particle impacts a surface, the incident particles can be reflected specularly, diffusely, or a combination of both.

Specular reflection ($\alpha_E = 0$) can be observed on smooth surfaces and implies an elastic collision in which the particle energy remains constant, whereas diffuse reflection ($\alpha_E = 1$) implies an exchange of transversal momentum that is determined by the surface temperature. Figure 2.5 represents both reflections. In specular reflections, the particle is reflected with the same angle of incidence while in diffuse reflections the angle of reflectance is determined by a Lambert cosine distribution.

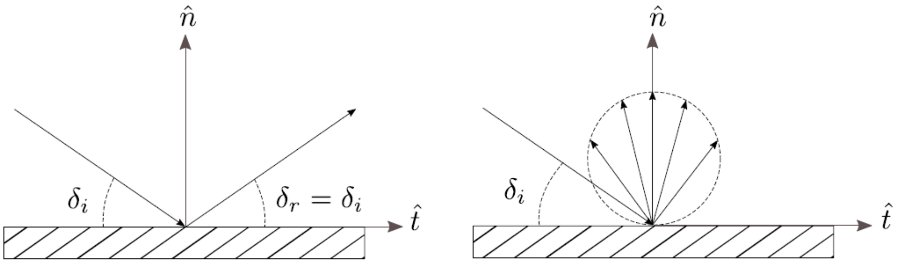

Figure 2.5: Representation of specular (left) and diffuse (right) reflections [13].

Adsorption of atomic oxygen onto spacecraft surfaces influences gas-surface interaction. More energy is lost to the surface by incident particles due to surface contamination. Therefore, the effects of atomic oxygen adsorption are the broader angular distribution of reemitted molecules, which is closer to the diffuse case, and higher particle accommodation to the surface. Thus, diffuse reflection with complete thermal accommodation can be assumed for altitudes lower than 300 km [14]. Note the utilization of materials that are resistant to the adsorption of atomic oxygen, along with the application of specialized finishes, can effectively reduce C_D [9].

Computational methods for analyzing the aerodynamics of a body in FMF, such as panel methods and Direct Simulation Monte Carlo (DSMC), involve high computational time. In the present study, the drag coefficient estimation is not carried out in order to save computational time. C_D is commonly assumed constant and equal to 2.2 in VLEO [9]. However, GOCE mission conducted in-flight measurements of C_D in this region and recorded a value much higher than 2.2. A value of $C_D = 3.7$ was measured and it is now assumed [15], [16]. This assumption shall compensate for neglecting the drag contribution of the parallel surfaces to the flow.

The expected experienced drag in VLEO for a spacecraft with a frontal area of 1 m^2 is depicted in Figure 2.6. In this analysis, it is assumed that the spacecraft is always perpendicular to the incoming flow, and parallel surfaces to the flow are disregarded in terms of their contribution to drag.

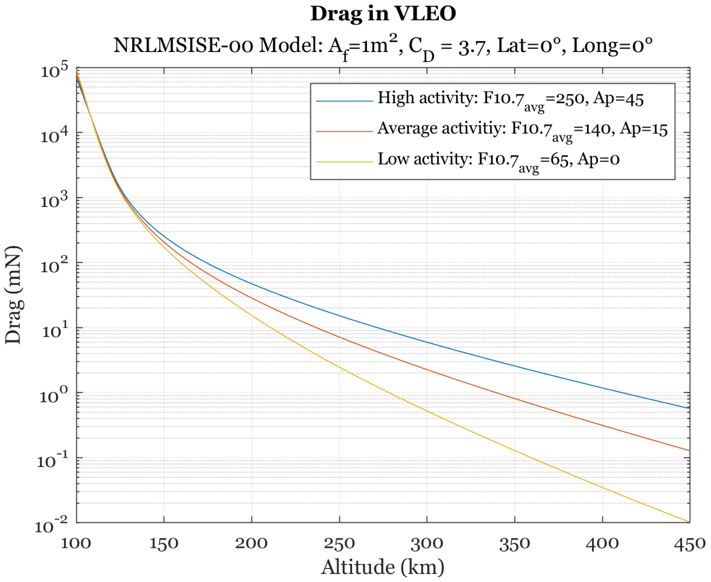

Figure 2.6: Experienced drag in VLEO.

As observed, solar activity directly affects atmospheric density, resulting in an elevation of experienced drag at a particular altitude. Consequently, solar activity plays a significant role in determining the viable range of operating altitudes.

2.3 Atmospheric model

The atmospheric properties in VLEO can be estimated using atmospheric models. Different atmospheric models of varying complexity and fidelity can be used with possible inputs dependent on geographic position, time, and space weather. ESA Space Environment Standard (ECSS-E-ST-10-04C) recommends NRLMSISE-00 and JB2008 models for characterizing the very-low environment [3]. Both models provide data on atmospheric temperature, total density, and the density of each atmospheric constituent. However, both models inherently present a degree of inaccuracy due to the complex and unpredictable nature of the atmosphere [12]. It is known that these models tend to slightly overestimate atmospheric density within $\pm 5\%$ with respect to actual density [17].

As NRLMSISE-00 is the most commonly utilized model in similar studies to this thesis, this model was selected for the present study. For clarification, NRL stands for Naval Research Laboratory, MSIS stands for Mass Spectrometer and Incoherent Scatter Radar and E indicates this model extends from the ground to space.

The model produces data on atmospheric properties from the surface to the lower exosphere (0-1000 km) regarding the effect of geographic position, day-night cycles, altitude, and solar activity. Optionally, it performs this calculation including contributions from anomalous oxygen (AO) that can affect satellite drag above 500 km.

Next in Chapter 4, NLRMSISE-00 model is implemented in MATLAB® to analyze the atmospheric drag experienced in orbit, which is influenced by the variation in atmospheric density.

To conclude, the characterization of the thermosphere is fundamental for assessing the feasibility of an ABEP spacecraft, as the performance of its thruster relies on the atmospheric parameters and the atmosphere is a complex and dynamic system. This way, every environmental parameter should be considered while designing an ABEP system.

Chapter 3

Air-breathing electric propulsion

Extensive research and technology development efforts are currently underway to tackle the critical challenges associated with VLEO operation. One area of focus is the investigation of novel materials that exhibit resistance to erosion caused by atomic oxygen and demonstrate specular GSI properties. By applying these materials in combination with aerodynamically optimized geometries, spacecraft would experience reduced drag, thereby extending their orbital lifetime. Aerodynamic geometries refer to forward-facing surfaces oriented at shallow angles to the oncoming flow. These geometries have the potential to generate lift forces enabling novel methods of aerodynamic attitude and orbit control. Beyond this, the development of air-breathing electric propulsion systems would enable sustained operation in VLEO, limited only by component lifetime [1].

The concept and working principles of air-breathing electric propulsion are introduced in this chapter. It begins with an overview of the electric propulsion fundamentals and, towards the end, the state-of-the-art of ABEP technology is presented.

3.1 Overview of space propulsion

Propulsion systems provide spacecraft with collision avoidance, orbital maneuvering, station keeping, orbit transfers, formation flight, and interplanetary trajectories using thrust. According to Newton's second law, thrust T is defined as the instantaneous force on the spacecraft that is proportional to the vector sum of the time rate of change of the momentum of the expelled propellant particles.

The specific impulse I_{sp} indicates the achievable change in momentum per ejected fuel mass. The I_{sp} characterizes the propellant consumption efficiency of the thruster. In general, the higher the I_{sp} the less propellant is required to achieve the same thrust [18]. The selection of an appropriate propulsion system involves a careful balance between various mission constraints, particularly considering the limitations associated with propellant mass.

Chemical propulsion uses chemical reactions (combustion) to release energy and accelerate gases through a nozzle to generate thrust. It can be divided into two categories: solid and liquid propulsion. Chemical systems produce a high level of T in relatively short periods of time (up to 1×10^7 N) making them widely used for launching satellites, spacecraft, and payloads into orbit or even beyond. However, their I_{sp} is low compared to other propulsion categories (up to $500\,\mathrm{s}$). These systems are not suitable for VLEO applications because of their significant weight, high cost, and limited operation lifetime as their fuel consumption efficiency is very low.

Nuclear propulsion consists of a nuclear reaction that heats the propellant and accelerates its ejection through the nozzle. It can be fission or fusion based, where fission is the splitting of an atom and fusion is the combination of them. This type of propulsion is considered a feasible option for crewed missions to Mars as it provides high T values (up to 1×10^6 N) and high $\mathrm{I_{sp}}$ (up to 1×10^5 s). However, it is unlikely that nuclear propulsion will be utilized in spacecraft due to safety concerns, such as the potential for explosions during lift-off, as well as the dissemination of radioactive materials, which would have harmful effects on living beings on the planet.

In propellant-less propulsion systems, thrust is generated by the interaction between the surrounding environment, such as solar pressure and planetary magnetic fields, and the spacecraft. For example, photon propulsion provides high $\mathrm{I_{sp}}$ (up to 3×10^7 s) but very low T values (up to 1×10^{-4} N). These systems are not suitable for near-space orbits as the environmental conditions would deorbit the spacecraft rapidly. However, they have great potential in interstellar traveling and asteroid detection.

Electric propulsion (EP) systems rely on electricity to ionize and accelerate the propellant out of the spacecraft and, hence, produce thrust. These systems can produce considerably high $\mathrm{I_{sp}}$ (up to 1×10^4 s) but low T (up to 100 N). Regarding the notorious $\mathrm{I_{sp}}$, EP is the most suitable solution for extended low-orbit operation [19]. Although electric thrusters may not generate high levels of thrust, they are still capable of generating sufficient thrust for drag compensation at these altitudes. Furthermore, these systems enable the reduction of the spacecraft launch mass leading to lower launch costs when compared to chemical propulsion.

3.2 Electric propulsion

Several missions have already demonstrated the effectiveness of electric propulsion in VLEO. The first mission orbiting this region was ESA's GOGE from 2009 until 2013. GOCE spacecraft carried out detailed measurements on the Earth's gravitational fields in altitudes between $230 - 280$ km. Drag compensation and orbit keeping was performed by an ion thruster until the stored xenon ran out.

The Tsubame spacecraft, part of JAXA's SLATS program, conducted experiments to evaluate the enhanced resolution of Earth's surface survey when operating at altitudes below $200\,\mathrm{km}$. The objective was to showcase the benefits of descending to lower orbits and demonstrate the advantages it offers in terms of Earth observation capabilities. Tsubame maintained its altitude at $167.4\,\mathrm{km}$ for a week using electric propulsion [14].

Both missions confirm that fuel mass storage is a key limiting factor for long-term orbit keeping in VLEO. Another notable example is the International Space Station (ISS) which maintains its orbit at $\approx 400\,\mathrm{km}$ by regularly receiving propellant through frequent resupplies [1]. Thus, air-breathing technology provides undoubted advantages as it uses the surrounding atmosphere as propellant.

The primary aim of SOAR mission was to characterize the aerodynamic performance of different materials at very-low altitudes. The materials carried to orbit were selected for their atomic oxygen erosion resistance. This mission is intended to improve the knowledge of the GSI and to identify novel materials that can minimize experienced drag at these altitudes [20]. The spacecraft used in the mentioned missions are displayed in Figure 3.1.

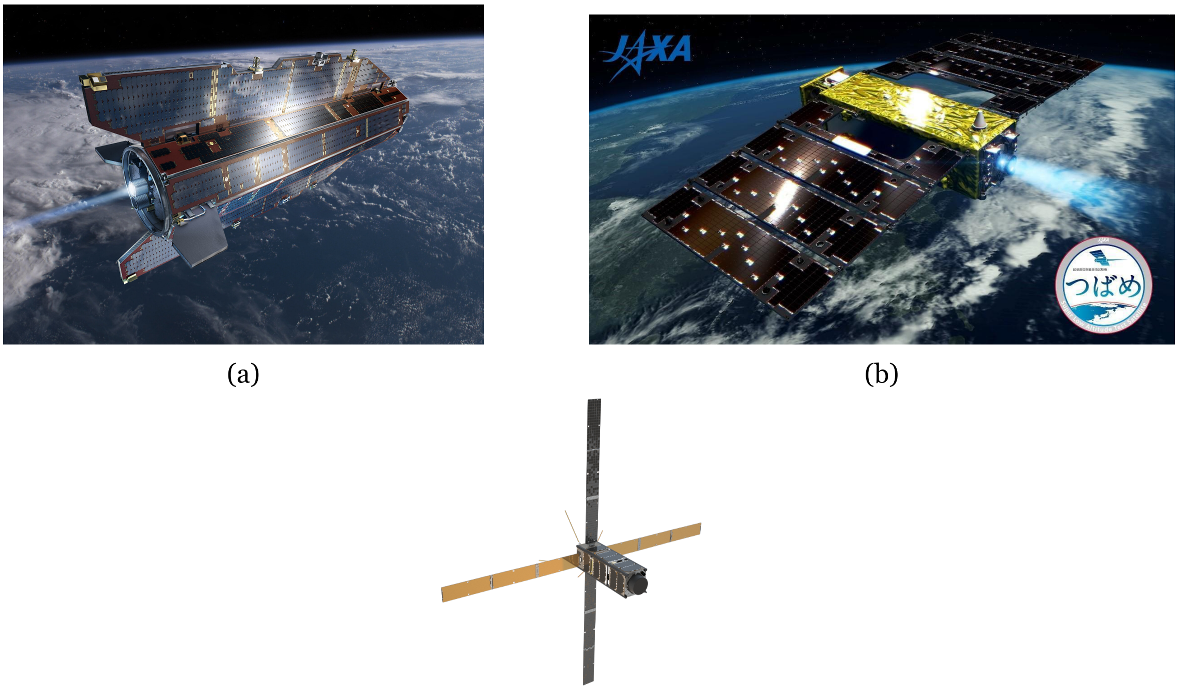

(a) (b)

(c)

Figure 3.1: (a) Goce spacecraft [21]. (b) Tsubame spacecraft [22]. (c) SOAR spacecraft [20].

Broadly speaking, EP encompasses any propulsion technology in which electricity is used to ionize and accelerate the propellant to generate thrust. When the propellant is ionized, it generates both ions and electrons, which collectively form plasma. The plasma is composed of a range of charged particles that can move freely in response to internally generated or externally applied electromagnetic fields. Despite the presence of charged particles, the overall electrical charge of plasma is nearly neutral [23].

The main metrics used to characterize electric thrusters are thrust T, specific impulse I_{sp}, and efficiency η_t that can be determined by Equations 3.1, 3.2 and 3.3, respectively.

$$T = \dot{m} v_e = \frac{2 \eta_t P_{in}}{I_{\mathrm{sp}} g_0} \quad (3.1)$$

$$I_{\mathrm{sp}} = \frac{T}{\dot{m} g_0} = \frac{v_e}{g_0} \quad (3.2)$$

$$\eta_t = \frac{P_{jet}}{P_{in}} = \frac{\frac{1}{2} \dot{m} v_e^2}{P_{in}} \quad (3.3)$$

Here, P_{in} is the input power, P_{jet} is the jet power, g_0 is the gravitational acceleration constant, $\dot{m}$ is the mass flow rate and v_e is the exhaust velocity [18] [24]. Thruster efficiency (η_t) measures the effectiveness of the thruster in converting the input power to the directed kinetic energy of the exhaust jet.

Electric thrusters can be divided into three major zones: the propellant storage (tanks), the ionization zone, and the acceleration zone. These systems can be classified according to the mode of operation (continuous or pulsed) or means of propellant acceleration (electrostatic, electrothermal, or electromagnetic).

For electrothermal thrusters, electric power is used to heat up the propellant which expands through a nozzle. This acceleration mechanism requires a relatively dense medium [14]. Traditional propellants used are hydrogen, xenon, hydrazine, ammonia, and other anaerobic propellants. There are two subcategories of this type of thrusters: arcjets and resistojets. Globally, the main drawbacks of these devices are the ablation of electrodes and the nozzle throat, and the achieved I_{sp} is limited to thermal heating. These thrusters were widely used in communications satellites. Nevertheless, the advancement of promising electrostatic thrusters has declined their potential applications.

For electrostatic thrusters, electric power is used to ionize the propellant, and an electrostatic field is used to accelerate it. Electrostatic systems are subdivided into different subcategories: electrospray thrusters (EST), gridded ion thrusters (GIT), and Hall-effect thrusters (HET). The most used propellants are liquid metals (indium, ceasium), xenon, krypton, and argon. Electrostatic engines are currently successful due to their promising performance and are applied in several space missions, e.g., in the Starlink constellation and GOCE mission. However, these thrusters also encounter the problem of plasma erosion that hinders the possibility of long-term missions.

For electromagnetic thrusters, electric power is used to ionize the propellant, and an electromagnetic field is used to accelerate it. It mainly includes pulsed plasma thrusters (PPT), magneto-plasma-dynamic thrusters (MPDT), and electrodeless thrusters. PPT is the only technology flight-proven in this category, used in station keeping and drag correction maneuvers. MPDT require high power which is unattainable for current spacecraft. Traditional propellants used are PTFE, helium, argon, and hydrogen, among others [19], [18]. Finally, electrodeless thrusters use directed plasma to propel spacecraft without employing electrodes that are prone to plasma erosion. These thrusters are still under development and aim to tackle the erosion problems [25]. Table 3.1 summarizes the performance of each electric propulsion system to further evaluate its feasibility for air-breathing applications.

Table 3.1: Performance of electric propulsion systems [19].

Category	Subcategory	I_{sp} (s)	T (mN)	P (kW)	η_t (%)	Propellant
Electrostatic	FEEP	8 k$\sim$12 k	0.001 $\sim$ 1	0.01 $\sim$ 0.15	30 − 90	In, Cs
	HET	1.5 k$\sim$2 k	80 $\sim$ 200	1.5 $\sim$ 5	50	Xe, Kr, Ar
	GIT	3 k	100 $\sim$ 200	0.5 $\sim$ 2.5	60 − 80	Xe
Electrothermal	Arcjet	500$\sim$2 k	200 $\sim$ 7000	0.3 $\sim$ 100	35	N_2H_4, NH_3
	Resistojet	300	100 $\sim$ 500	0.5 $\sim$ 1.5	80	N_2H_4, NH_3
Electromagnetic	PPT	1k	1 $\sim$ 100	0.001 $\sim$ 0.2	5	PTFE, Ar
	MPD	2 k$\sim$5 k	1 $\sim$ 200 N	1 $\sim$ 4000	25	NH_3, H, Li

3.3 State-of-the-art

ABEP proposes the use of a forward-facing intake that collects the propellant from the residual atmosphere that is subsequently used by an electric thruster, eliminating the need of carrying onboard propellant. Furthermore, this technology has the potential to be applied in the atmosphere of other planetary bodies, such as Mars [24]. It is possible to single out five main elements of these thrusters [14]:

- an air intake that ensures the collection of atmospheric gas.

- a thermalizer (accumulator) in which the gas is decelerated to thermal velocities.

- an ionization stage in which the gas is ionized.

- an acceleration stage in which the ionized gas is accelerated by an electromagnetic field.

- a neutralizer of the plasma jet.

The last three elements require electric power for their operation which source can be a combination of solar arrays and batteries [26]. In a broader sense, the components of air-breathing electric thrusters can be categorized into three principal systems: the intake system, the thruster system, and the power source system as depicted in Figure 3.2. The intake system comprises the intake and the accumulator while the thruster system comprises the remaining enumerated components.

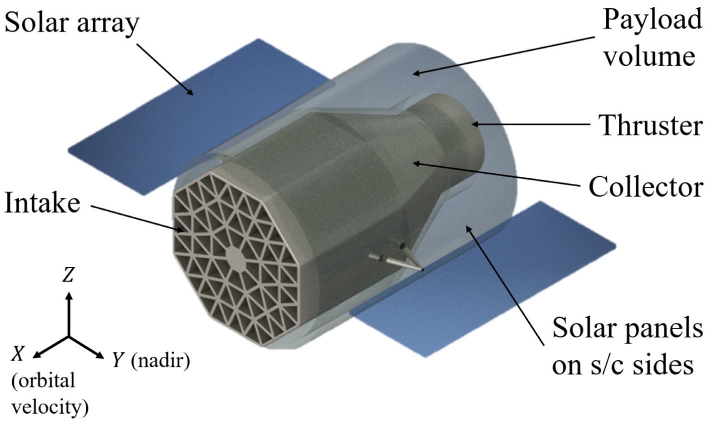

Figure 3.2: Schematic of an ABEP system [12].

ABEP and EP systems have common features as significant differences. The primary difference is the propellant supply (collection or storage). Air-breathing thrusters collect the residual atmospheric particles for use as propellant, whereas traditional thrusters carry onboard propellant tanks. Consequently, ABEP relies on factors such as atmospheric collection efficiency and orbital conditions, whereas traditional electric propulsion systems rely on predetermined propellant chemical composition and pressure throughout their operation.

Besides, atmospheric species (N_2, O, O_2) have an average atomic/molecular mass lower and ionization energy higher than traditional propellants used in EP, such as Xe. Lower molecular mass imparts less momentum to the exhaust jet and higher ionization energy requires more energy to ionize the propellant. To illustrate this point, Table 3.2 compares the characteristics and performance of atmospheric species to noble gases. These conditions contribute to a decrease in the performance of ABEP when compared to EP [14].

Air-breathing technology is only a competitive solution within an altitude range of $160-250$ km. The upper limit is determined by the minimum air density required for plasma ignition, while the lower limit is constrained by the thruster capability to overcome drag [12].

Table 3.2: The characteristics of atoms and molecules in the upper atmosphere compared with noble gases [27].

Species	Atomic/molecular mass (g/mol)	1^{st} ionization potential (eV)	Exhaust velocity (1500 V) (km/s)
O	15.999	13.618	134
O_2	32.0	12.2	95
N_2	28.016	15.58	102
CO_2	40.02	13.7	85
Ar	39.95	15.76	85
Xe	131.30	12.13	47

3.3.1 ABEP systems

A plethora of institutions and companies are researching and designing ABEP systems for VLEO applications. Most of the studies use traditional electric thrusters such as HET and GIT due to their potential performance. However, the need to address the challenges associated with the erosion caused by atmospheric propellants spurred the exploration of electrodeless thrusters. Prior to introducing the proposed ABEP concepts, a brief explanation of such propulsion systems is presented.

HET utilize an electrostatic field to accelerate propellant. This field is generated by an externally positioned cathode and an internally positioned anode ring. The cathode supplies electrons that attempt to reach the anode, but they encounter a radial magnetic field induced by magnetic coils, which reduces their axial mobility and hinders their flow towards the anode. Propellant is introduced into the discharge chamber and becomes ionized upon colliding with the spinning electrons. The plasma, thus formed, is accelerated by the electrostatic field, and some electrons provided by the cathode also depart from the thruster to neutralize the ion beam. Figure 3.3a provides a schematic illustration of a HET to facilitate a clearer understanding of its operational principles. Certain thrusters incorporate an additional stage responsible for ionizing the propellant using microwave energy, such as an electron cyclotron resonance (ECR) source. These devices operate without relying on electrodes, which are susceptible to erosion caused by atomic oxygen.

GIT are also electrostatic thrusters. The propellant is injected into the discharge chamber and typically ionized by electron bombardment. The generated plasma is further accelerated by electrostatic grids and the ion beam is neutralized by a neutralizer mounted outside the thruster. Energetic electrons can be emitted by a hollow cathode and then accelerated towards the anode, a configuration known as the Kaufman type. Alternatively, propellant ionization can be achieved through electromagnetic fields generated by a radiofrequency (RF) coil, followed by acceleration through grids. Notably, this mechanism operates without the need for electrodes and is defined as a radiofrequency ion thruster (RIT). Figure 3.3b provides a schematic illustration of the working principle of a GIT.

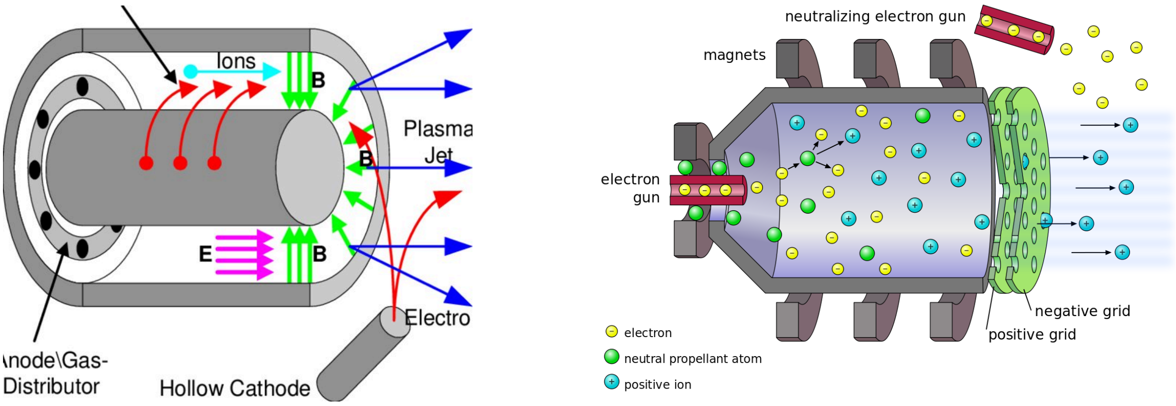

(a) (b)

Figure 3.3: Schematic drawing of (a) Hall-effect thruster [28] (b) gridded ion thruster [29].

Finally, electrodeless thrusters encompass various types of electromagnetic thrusters, with inductive plasma thrusters (IPT) being one such variation. These thrusters inject propellant into a discharge chamber which is wrapped on a radiofrequency-fed coil. The propellant is ionized and accelerated by the oscillating electromagnetic field created by the coil. Since the process is electrodeless, any gas can be used. Moreover, there is no need for a neutralizer as the plume is charged neutral [19]. These thrusters hold significant promise, although their development is still ongoing.

At first, Japan Aerospace Exploration Agency's (JAXA) proposed a concept named Air-Breathing Ion Engine (ABIE) composed of an intake, a discharge chamber (plasma generator), grids (ion beam acceleration), and a neutralizer. The concept uses a microwave-emitting antenna to generate an electric field, and magnets to produce a strong magnetic field. The electric and magnetic fields ionize the propellant to be further accelerated by a set of grids. ABIE scoops up atmospheric particles traveling at $\approx 8\,\mathrm{km/s}$, ionizes them by means of ECR, and accelerates them electrostatically to exhaust velocities of $\approx 30\,\mathrm{km/s}$. The key technology of this thruster is the design of the intake. The concept is considered feasible in an altitude range of $150 - 200$ km and presented in Figure 3.4a [27].

European Space Agency (ESA) studied the feasibility of an ABEP system for very-low Earth observation missions. The concept includes a collection system to capture the atmosphere and four GIT to generate thrust. The intake is positioned in the axial direction of the spacecraft and presents a honeycomb shape. The study concluded that the concept has great potential for long-life missions within $200 - 250$ km of altitude and for lifetimes of $3 - 8$

years. However, thruster performance was predicted using theoretical models. The thruster of nitrogen-oxygen mixture still needed to be tested and verified in order to verify its feasibility [30]. ESA's concept is shown in Figure 3.4c.

Years later, ESA began with a test campaign of a GIT and a HET with non-conventional propellant. Table 3.3 summarizes the results, however, it is important to emphasize that propellant conditions only reflect atmospheric composition at specific altitudes. Moreover, the thrusters were originally not designed for non-conventional propellants, although they underwent minor modifications to enhance performance. For example, RIT-10-EBB includes water cooling as higher power consumption and temperatures are expected during operation [31].

The results emphasize the reduced performance of ABET as indicated by the reduction of η_t. During the tests, grids experienced erosion while operating with oxygen. However, long-firing tests demonstrated that both devices were capable of continuous and stable operation with atmospheric propellant. It was concluded that HET is preferable when a high thrust-to-power ratio T/P is required, while RIT is more suitable when low thrust levels are needed [31].

Table 3.3: Experimental characteristics of EP with atmospheric propellant.

Thruster (type)	Gas mix	T (mN)	$\dot{m}$ (mg/s)	$\dot{v}$ (sccm)	P (W)	I_{sp} (s)	T/P (mN/kW)	η_t	Ref.
PPS1350-TSD (HET)	Xe	≈ 40	2.86 mg/s	-	≈ 775	-	$\approx 51^c$	-	[31]
	N_2	21	2.65 mg/s	-	1000	-	21	-	
	$1.27N_2 + O_2$	24	2.75 mg/s	-	1000	-	24	-	
RIT-10-EBB (RF GIT)	Xe	15.1	-	3.2 sccm	600	4879	25.1	0.6	[12], [31]
	N_2	7.43	-	6.0 sccm	570	5306	13.0	0.34	
	O_2	6.95	-	6.8 sccm	610	5011	11.4	0.28	
	$0.56N_2 + 0.44O_2$	7.16	-	6.0 sccm	560	5455	12.8	0.34	

^{c}: calculated value.

Busek Co. demonstrated and tested an ABET concept for application in the Martian atmosphere. The thruster was named Martian Air-Breathing Hall-Effect Thruster (MABHET) and is represented in Figure 3.4b. The company tested an unmodified HET (designed to operate with Xe) with a gas mixture reproducing the Martian atmosphere, mainly constituted of CO_2. The study concluded the thruster may actually be able to compensate for the Martian drag [32].

The European DISCOVERER Consortium of various universities and companies developed a concept consisting of an intake and a RF helicon-based plasma thruster (HPT), especially suited to survive long time exposure to chemically aggressive species, like atomic oxygen in VLEO with its electrodeless thruster design [16]. IPT concept is depicted in Figure 3.4d.

Lastly, the European AETHER Consortium also contributed by designing and evaluating a concept involving a passive intake and a double-stage HET, depicted in Figure 3.4e. Sitael, an Italian company, led the way by becoming the first institution to test an ABEP system within a simulated VLEO environment. The experimental set-up encompassed a particle flow generator, which supplied the ABEP system with a high-speed flow reproducing in-orbit conditions at a reference altitude of 200 km. The particle flow generator consisted of a HET fed by a N_2/O_2 mixture.

Table 3.4: Conceptual projects of spacecraft with ABEP.

Institution	Type	Altitude (km)	Intake	β	η_c	η_t	I_{sp} (s)	T (mN)	Power (W)	Ref.
Jaxa/ABIE	ECR+GIT	150 – 200	passive	-	-	-	3000	-	3300	[27]
ESA/RAM-EP	RIT-10	200 – 250	passive	-	-	-	-	2 – 20	1000	[30]
Busek/ MABHET	HET	160	passive	250	0.25 – 0.33	0.25	-	46.5^c	1500	[32]
Sitael/RAM-EP	2-stage HET	200	passive	95 – 140	0.28 – 0.32	-	-	6	900^c	[33]
Un. of Stuttgart/IPT	HPT	200	passive	-	0.43	0.2	3400		4670	[24]

^{c}: calculated value.

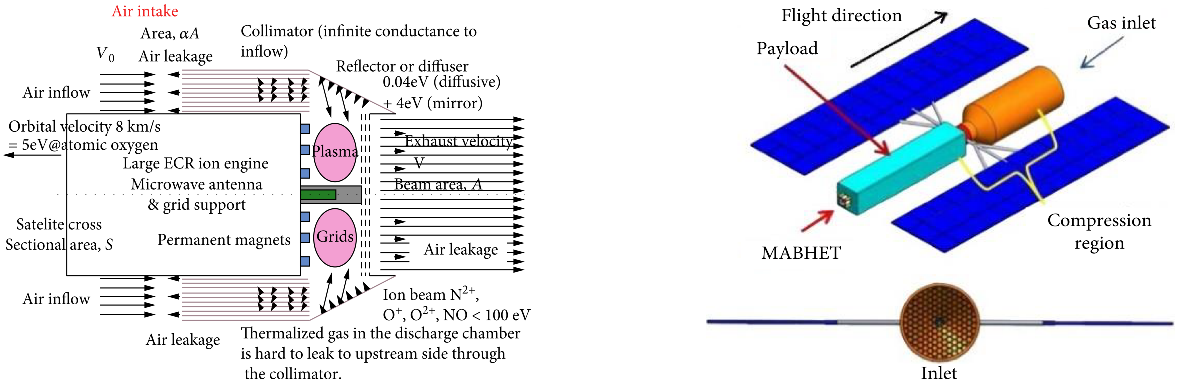

(a) JAXA's concept: ABIE [27].

(b) Busek's concept: MABHET [19].

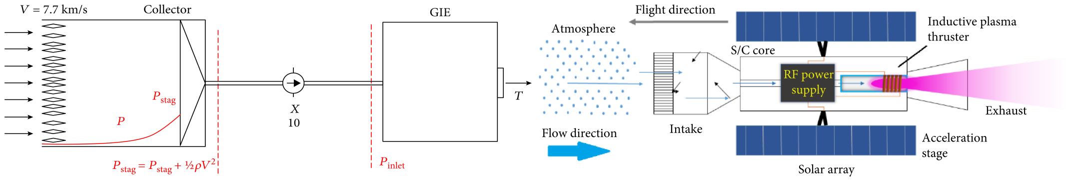

(c) ESA's concept [30].

(d) DISCOVERER's concept [19].

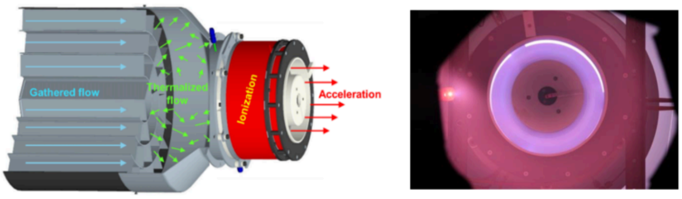

(e) AETHER's concept [24].

Figure 3.4: Air-breathing electric systems concepts.

Table 3.4 summarizes the characteristics of the enumerated concepts. While significant research efforts are currently ongoing, the highlighted concepts were specifically selected for their experimental progress. However, ABEP technology is not been flight-proven yet.

3.3.1.1 Intake

The intake subsystem is responsible for collecting and compressing the airflow, allowing the system to orbit at higher altitudes than 150 km since the required operating pressure is provided at altitudes bellow. Effective thruster operation requires a minimum propellant pressure generally higher than 10^{-5} mbar [2]. Thus, the propellant number density at the thruster inlet must be $\geq 10^{18}$ m^{-3} for plasma ignition and stable burning at the ionization chamber [14]. Figure 2.2 indicates that this value is not achieved at altitudes higher than 150 km ($n \leq 10^{16}$ m^{-3}). Therefore, the surrounding air should be compressed at least $100-200$ times for plasma ignition. A fairly complete review of the most recent developments in intakes is presented in [3]. Intake performance is often evaluated in terms of collection efficiency and compression factor.

Collection efficiency η_c represents the ratio of mass flow rates between the onset flow at the intake entrance and the thruster. Typical η_c values range from $0.3-0.5$. The compression factor β represents the density ratio between the intake exit and entrance. Typical β assumes values between $95-140$ [12].

The intake task is hampered in VLEO due to its unique environmental characteristics. The low-density atmosphere makes it arduous to attain high collection efficiencies, mainly because the collection of air is not uniform or consistent. In this environment, gas molecules move independently, and their paths may not be predictable, which can lead to issues like particle backflow.

η_c is considered one of the most significant metrics to access lower altitudes. Increasing η_c leads to a larger $\dot{m}$ available for the thruster and thus more T generated, lowering the required $\mathrm{I_{sp}}$. However, higher η_c leads to a diminished β, thereby diminishing the maximum achievable operational altitude due to declining density and the subsequent need for greater compression. Consequently, the design of an intake can be tailored to target higher or lower orbital altitudes by manipulating these parameters. Lower altitudes require higher η_c for drag makeup, while higher altitudes require higher β due to density drop-off [12]. There are two different approaches in terms of design for increasing air density: active compression and passive compression.

Passive intakes compress the incoming flux by rarefied gas-dynamic processes. These processes can result in an increase of up to two orders of magnitude in pressure at the thruster inlet, compared to the ambient conditions. In passive compression, η_c and β are strongly related. Increasing the η_c usually reduces the β, and vice-versa. Considering that $\beta > 100$ is required to operate at altitudes higher than 150 km, passive intakes prove to be feasible mechanisms for air compression as they achieve the required compression factors. However, their compression capability is limited which in turn limits the operational upper altitude for ABEP systems ($\approx 250\,\mathrm{km}$).

The inclusion of an active compression stage enables the increment of β, while keeping high η_c. Moreover, active compression allows the storage of the collected propellant and hence, the decoupling of the thruster operation from the propellant collection. Compared with passive intake devices, active designs can provide an extremely high compression performance. However, such a demanding design with complex active mechanical and heavyweight devices still needs to be optimized for space applications, particularly due to the utilization of turbomolecular pumps for active compression [2].

The significant challenge posed by ABEP technology revolves around the collection and compression of atmospheric gases to generate thrust. The intake component currently remains the least developed as it is a novel addition to this technology. Although Sitael's intake has been tested, further development is needed. Table 3.5 summarizes the research efforts on air intakes.

Table 3.5: Previous studies about intake designs [3].

Institution	Configuration	Length (m)	Inlet area (m^2)	Altitude (km)	Style	Scattering	η_c	β
JAXA	Ring collimator with ducts; Reflector	$0.8 - 2.91$	0.48	$180 - 220$	Passive	Diffuse	< 0.46	< 180
ESA	Grid system; Long collector	$0.2 - 1.3$	< 0.6	$200 - 250$	Passive	Diffuse	-	≈ 10
BUSEK	Honeycomb ducts; Long cylinder	3.7	< 0.2827	$120 - 180$	Passive	Diffuse	$0.2 - 0.4$	250
Lanzhou	Multi-hole plate; Active pump; Gas chamber	> 0.16	0.1865	$150 - 240$	Active	Diffuse	0.67	$2.7e5$
U. Colorado	Parabolic chamber	$0.05 - 0.1$	0.0078	$100 - 300$	Passive	Diffuse; Specular	$< 0.1; > 0.9$	-
U. Stuttgart	Haxogonal intake and ducts; Tapered chamber	≈ 0.09	0.004	$150 - 250$	Passive	Diffuse	0.458	< 4
TsAGI	Parabolic chamber; Square inlet ducts; Accumulator	≈ 0.28	0.019	$150 - 250$	Passive	Specular	0.943	< 641
		≈ 0.1	< 0.0078	$160 - 200$	Passive	Diffuse	$0.33 - 0.34$	< 500
SITAEL/VIK	Split-ring ducts, Conical interface	≈ 1	< 0.7854	$180 - 250$	Passive	Diffuse	$0.28 - 0.3$	$95 - 140$
NUDT	Honeycomb ducts; Parabolic chamber; Diffuse tube	0.13	0.6467	200	Passive	Specular + Diffuse	0.6579	210.2

As predicted, the best β performance is achieved by active devices. However, these systems rely on electric energy, making them less suitable for missions with power constraints. The available solar energy may not be able to provide sufficient power supply for both pump and electric propulsion systems. It is worth noting that passive intakes do not demand electrical power for their operation, therefore, they are the most appropriate solution for ABEP application to date. An active intake is represented in Figure 3.5a. In summary, the state-of-the-art intake systems are capable of achieving approximately $\beta \approx 140$ and $\eta_c \approx 0.3$, based on experimental tests.

Passive designs generally include inlet ducts, a tapered chamber, and a tube to the electric thruster. Presented below are the outcomes derived from the studies featured in Table 3.5, which were focused on enhancing intake performance.

A long and narrow design is proven to reduce the particle's backflow effectively and achieve higher η_c. This way, different duct cross-section configurations were studied, including hexagonal (honeycomb), cylindrical, annular, square, split-ring types, and so on. Most institutes believe that the honeycomb design is the most promising among them due to its superior performance. In addition, the aspect ratio of ducts must be optimized for each intake design. Figures 3.5b, 3.5c and 3.5d depict different configurations.

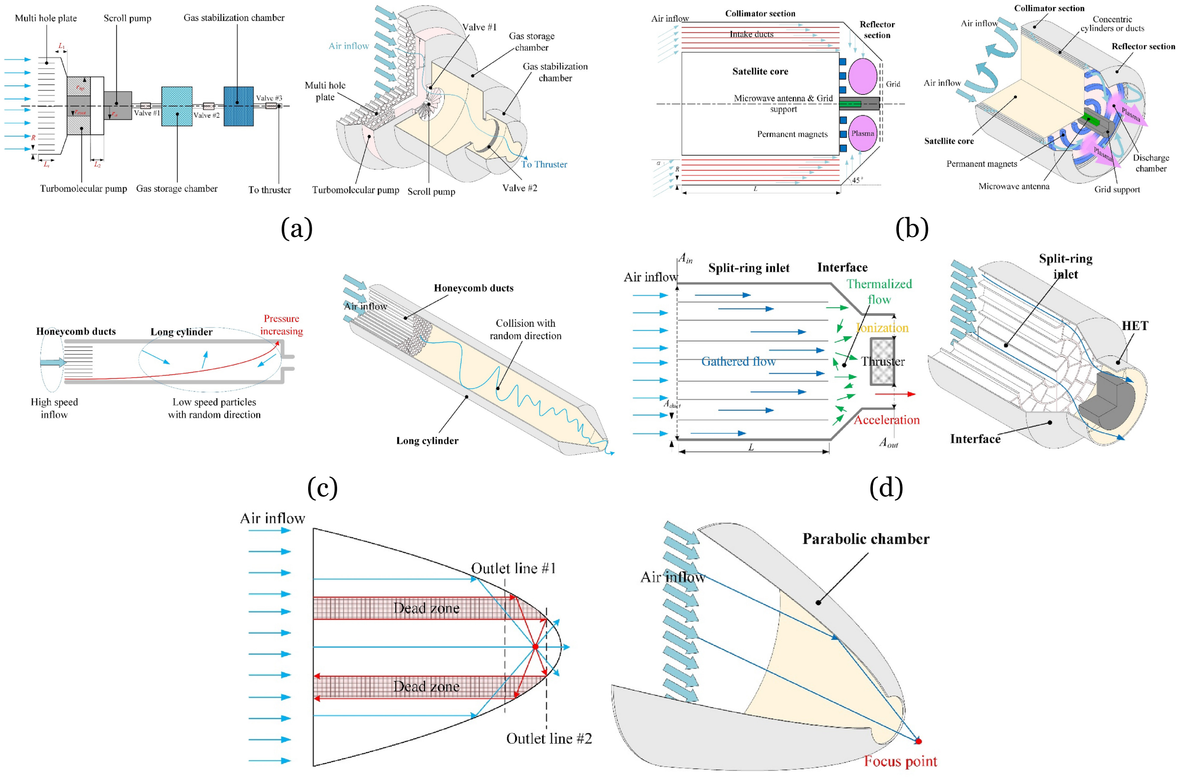

(a) (b)

(c) (d)

(e)

Figure 3.5: (a) Active intake by Lanzhou Institute of Space Technology and Physics. (b) Passive intake by JAXA. (c) Passive intake by Busek. (d) Passive intake by Sitael. (e) Passive intake by NUDT [3].

Due to the same particle number in a smaller volume, a tapered chamber also demonstrated the ability to attain higher input number density. Three different inlet shapes were studied and analyzed: pyramidal, conical, and parabolic inlets. According to the findings, the parabolic shape outperforms the other two, under the ideal scenario of specular reflection, due to its optic properties that reflect all the particles toward the focus of the parabola. However, the flow's number density needs to be increased because its compression performance is too low. A diffuse reflection tube can be seen as the solution to improve β and optimize parabolic intake design. Figure 3.5e represents a parabolic chamber.

To date, an intake featuring honeycomb inlet ducts, a parabolic chamber with a specular wall, and a diffuse reflection tube seems to achieve better performance (higher η_c and β). However, the design has not been validated experimentally and suitable materials must be identified to retain the reflection properties of the intake surface under the atomic oxygen corrosion in VLEO.

3.3.1.2 Thruster

The thruster system can be divided into two plasma stages: the generation and the acceleration stages, even though they can be blended into one. The performance of traditional electric thrusters operating with atmospheric propellant and conceptual ABET was already presented in Tables 3.3 and 3.4.

A potential thruster for air-breathing applications is one that allows long-term maintenance in VLEO (high I_{sp} required) and drag compensation (appropriate T) while operating with the atmospheric medium. From Table 3.4, it is observed that electrostatic and electromagnetic thrusters are the most considered thrusters for air-breathing applications.

The operation of electrothermal thrusters (resistojets and arcjets) in VLEO is improbable due to the presence of chemically active propellants that can react with the components (electrodes, resistors), leading to degradation in their performance. Additionally, the low I_{sp} of resistojet is a decisive disadvantage when considering ABEP application [19].

Regarding electromagnetic thrusters, the required flow rates for magnetic-dynamic ones may be too high for low-orbit applications [19]. Another drawback is the required power that would demand large solar panels, thereby increasing the spacecraft's mass and aerodynamic drag. Concerning pulsed-plasma thrusters, despite their minimal power-consumption and successful tests with gaseous propellants, their comparatively low I_{sp} greatly reduces their application for the purpose [14]. Electrode corrosion is also an issue faced by electromagnetic thrusters. As a result, electrodeless thrusters have emerged as a promising solution, however, they are still at a relatively low level of maturity.

Among electrostatic thrusters, electrospray thrusters are not appropriate since they operate with ionic liquid propellant, demanding further complexity for implementing atmospheric gases in the system. Despite their high I_{sp}, these thrusters offer very low thrust values, making them unsuitable for the applications. Both Hall-effect and gridded ion thrusters are of interest for air-breathing applications regarding their high I_{sp} and potential T/P [14]. Based on Tables 3.3 and 3.4, ABET concepts can currently provide a thruster efficiency, thruster density, and specific impulse up to 0.35, $24\,\mathrm{mN/kW}$ and $5455\,\mathrm{s}$, respectively. In Chapter 4 the development of an application able to compute the required T, I_{sp} and P_{in} for a given air-breathing mission is conducted.

3.3.1.3 Power

The power system provides electrical power P to all the subsystems of the spacecraft. Typically, solar panels and batteries are used as power sources. The batteries are employed when the solar arrays (SA) are not exposed to sunlight. Based on literature, the nominal specific power per panel area is considered $a_p \approx 368$ W/m^2 [12].

Body-mounted solar panels are preferred for minimizing experienced drag, even though certain panels may not be fully illuminated or operating at peak efficiency. Deployable solar panels are favored to meet the necessary energy demands, despite their contribution to aerodynamic drag. Therefore, the optimal orientation relative to the direction of the Sun is significantly limited. As an example, GOCE spacecraft presented 4 m^2 body-mounted panels and 5 m^2 of wing-mounted panels [12].

A key aspect of flight in VLEO is the provision of electric power by solar arrays. The most optimal solar arrays illumination conditions are observed in sun-synchronous orbits (SSO) [14]. Furthermore, this type of orbit is also beneficial for Earth observation applications as the spacecraft revisits the same spot at the same local time, enabling effective comparison and analysis of changes [21].

3.3.2 Sun-synchronous orbits

Broadly defining, SSO are understood to be near polar orbits whose nodal precession rate matches the Earth's mean orbital rate around the Sun providing desirable exposition characteristics for ABEP operation. Since the orbital inclination is nearly polar ($i \approx 90°$), it provides almost global coverage at all latitudes. Additionally, solar exposure maintains approximately constant throughout the mission as the position of the line of nodes remains roughly fixed with respect to the sun's direction. This type of orbit is represented in Figure 3.6.

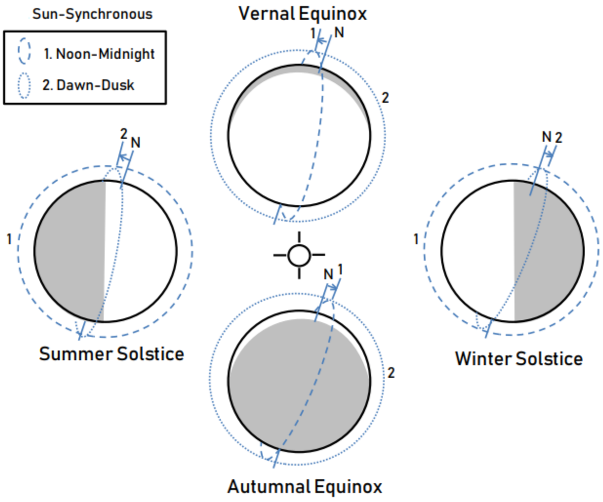

Figure 3.6: Sun-synchronous orbit [34].

To provide a comprehensive definition of SSO, it is necessary to begin with a review of the fundamental principles of orbital mechanics and how they are influenced by Earth's shape. An ideal Keplerian orbit is described by:

$$\ddot{\vec{r}} = \frac{-\mu \vec{r}}{r^3} \qquad (3.4)$$

where $\vec{r}$ is the position vector of the spacecraft and μ is Earth's gravitational parameter. However, external perturbing forces cause deviations from the ideal orbit that result in time-varying orbital elements.

Orbital elements provide a framework for characterizing and understanding the path a celestial object takes around a central body and are defined in Figure 3.7.

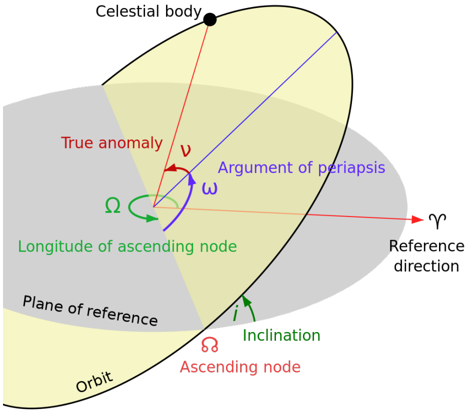

Figure 3.7: Keplerian elements [35].

where the inclination i measures the angle between the orbital plane and the equator plane, the right ascension of the ascending node Ω or $RAAN$ defines the orientation of the ascending node of the ellipse with respect to the reference frame's vernal point Υ, the argument of the perigee ω defines the orientation of the orbital ellipse in the orbital plane, and the true anomaly υ indicates the position of the orbiting body along the ellipse at a specific time. Additionally, the semi-major axis a defines the orbit size, and the eccentricity e indicates the deviation of the trajectory from a circle. The orbital period T_o and the period's ratio in which the satellite is illuminated are given by [36]:

$$T_o = 2\pi\sqrt{\frac{a^3}{\mu}} \quad (3.5)$$

$$\frac{t_{sunlight}}{T_o} = \frac{\pi + 2\arccos\frac{a_e}{a}}{2\pi} \quad (3.6)$$

where a_e is considered the equatorial radius of the Earth ($\approx 6378\,\mathrm{km}$). Despite being a SSO that offers optimal illumination conditions, there are still periods during each orbit when the spacecraft is not exposed to sunlight.

Real orbits experience perturbations that render the two-point mass approximation provided by Equation 3.4 invalid. These perturbations arise from various sources, including: non-spherical shape of the Earth, gravitational effects of other bodies (especially the Moon and the Sun), solar radiation, and atmospheric drag [37]. A real orbit can be described as follows:

$$\ddot{\vec{r}} = \frac{-\mu\vec{r}}{r^3} + \vec{a_p} \quad (3.7)$$

where $\vec{a_p}$ is the perturbation acceleration. For simplicity, only the non-spherical Earth's perturbation is considered for this study.

As discussed in Chapter 2, the motion of spacecraft in VLEO is primarily influenced by two key perturbations. The first is the primary-gravity which considers a constant gravitational acceleration vector $\vec{g}$. The second perturbation, known as J_2, accounts for the effect of Earth's oblateness caused by its rotational motion. The Earth exhibits a bulge at the equator, with a radius $\approx 20\,\mathrm{km}$ larger than at the poles [37].

The shape of the Earth is defined by its gravitational field and not by its topography. The gravitational field is expressed by equipotential surfaces that are always perpendicular to the direction of gravity. This way, the realistic shape of the Earth is a geoid. A geoid is an equipotential surface that closely approximates the mean sea level under the influence of Earth's gravitational field as depicted in Figure 3.8 [38]. It is important to note that the geoid is not the same as the Earth's actual physical surface.

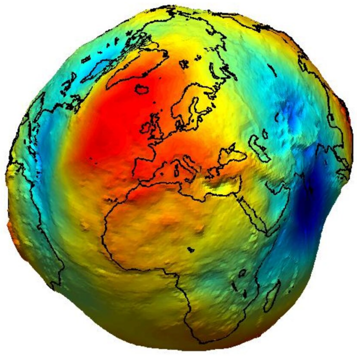

Figure 3.8: Earth geoid [39].

Its irregularity and, consequently, complexity are mainly due to the uneven distribution of mass of the Earth. Therefore, it is necessary to approximate the geoid by a surface that can efficiently be handled mathematically. Generally, an ellipsoid of revolution (or spheroid) is adopted in order to consider the flattening, represented in Figure 3.9a. The World Geodetic System 1984 (WGS84) is one of the various global Earth models and is the nominal reference ellipsoid used by the Global Positioning System (GPS).

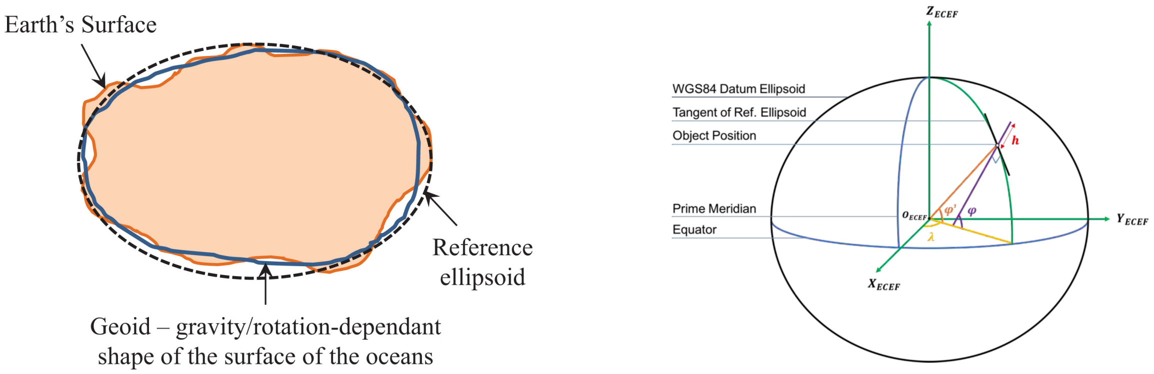

(a)

(b)

Figure 3.9: (a) Several ellipsoids approximating the geoid [40]. (b) Ellipsoidal coordinate system [41].

A coordinate system is a methodology to define the location of a spacecraft in space. On an ellipsoidal system, positions are either expressed in Cartesians coordinates (X, Y, Z) or in spherical coordinates (ϕ, λ, h), i.e., geodetic latitude, geodetic longitude, and ellipsoidal height. In a geocentric Cartesian coordinate system, the Z-axis coincides with the Earth's rotation axis, X-axis passes through the intersection of the Greenwich meridian and the equator, and the Y-axis is defined by the right-handed rule. Both coordinate systems are represented in Figure 3.9b [38].

In simple terms, Earth's asymmetry creates an out-of-plane gravitational force on the spacecraft's orbit causing it to gyroscopically precess. This perturbation leads to time-varying rates of change in all orbital elements. However, in a circular orbit, only Ω experiences change as $e = 0$, $\dot{a} = 0$, and ω is undefined since there is no perigee.

SSO are made possible by this rate of change ($\dot{\Omega}$) as it ensures the orbital plane precession. Without this precession, the orbital plane would remain fixed and not maintain its synchrony with the Sun. The rate of change of Ω owing to J_2 perturbation is defined as:

$$\dot{\Omega} = -\frac{3}{2} J_2 \frac{{a_e}^2}{p} n \cos(i) \quad (3.8)$$

where $p = a(1 - e^2)$ is the orbit parameter, $n = \sqrt{\frac{\mu}{a^3}}$ is the mean motion, and $J_2 = 1.082\,63 \times 10^{-3}$ is the zonal harmonic coefficient. Thus, the nodal precession rate is a function of the three classical orbital elements a, i and e, and can be manipulated by selecting the proper orbital elements. Note that for a circular orbit $p = a$.

The condition for an orbit to be SSO is that the precession rate equals the Earth's mean motion, under the assumption the Earth's orbit around the Sun is circular with a period of one year:

$$\dot{\Omega} = \frac{360}{365.242199} = 0.986°/\text{day} = 1.991 \times 10^{-7} \text{rad/s} \quad (3.9)$$

Circular orbits reduce the precession rate dependency only to orbital inclination and altitude ($h = a - a_e$). This way, the specification of the desired orbital altitude yields the inclination automatically. Figure 3.10 displays the required inclination for an orbit to be sun-synchronous at various altitudes.

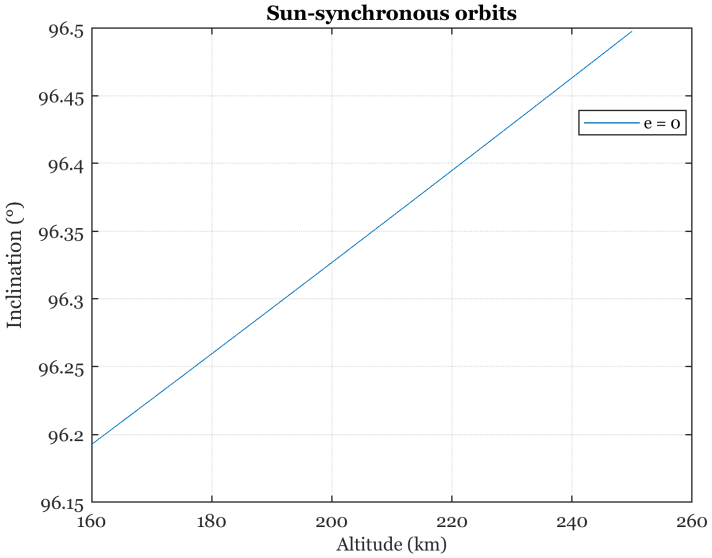

Figure 3.10: Sun-synchronous orbit inclination for different altitudes.

It is important to stress that for $i < 90°$ the node regresses, i.e., rotates clockwise as seen from the north, and for $i > 90°$ the nodal motion is posigrade, i.e,. precesses counter-clockwise as seen from the north [42].

Chapter 4

App development

The main goal of the present work is to create an app capable of calculating the required propulsive performance for maintaining a spacecraft in VLEO utilizing an ABEP system. The outcomes of the app will offer valuable insights into the feasibility of conducting very-low missions with air-breathing technology.

The app is designed to receive specific mission parameters (orbital altitude, start time, duration) and the spacecraft's geometry (frontal area) as inputs. With this information, it can accurately calculate the necessary thruster performance to maintain the spacecraft's orbital altitude by compensating for drag during the mission. Also, the user has the option to select air-breathing system specifications (collector efficiency, thruster efficiency) and the drag coefficient. The default values for these parameters are $\eta_c \approx 0.3$, $\eta_t \approx 0.35$, and $C_D = 3.7$. In the previous chapter, these values were identified to be representative of the achievable performance of air-breathing technology and the most appropriate drag coefficient to describe the very-low environment. This chapter also highlighted the benefits of sun-synchronous orbits for air-breathing applications, making them the focus of the app. For simplicity, circular orbits will be assumed.

The process for achieving the desired outputs is illustrated in Figure 4.1. The application has been developed using MATLAB®, taking advantage of its features throughout the process. To calculate the required conditions for altitude keeping, it is crucial to determine the drag experienced by the spacecraft. This involves identifying the atmospheric properties along the orbit. Consequently, the position of the spacecraft over time, known as the ephemeris, must be obtained. The processing blocks have been designed to address these aspects and ensure accurate calculations. Hereby, the process flowchart is represented and explained in more detail.

4.1 Sun-synchronous orbit block

This block calculates the Keplerian elements of a sun-synchronous orbit for a given orbital altitude (h) and mission start time. According to Equation 3.9, the orbital plane must precess approximately 1° each day to be synchronous with the sun.

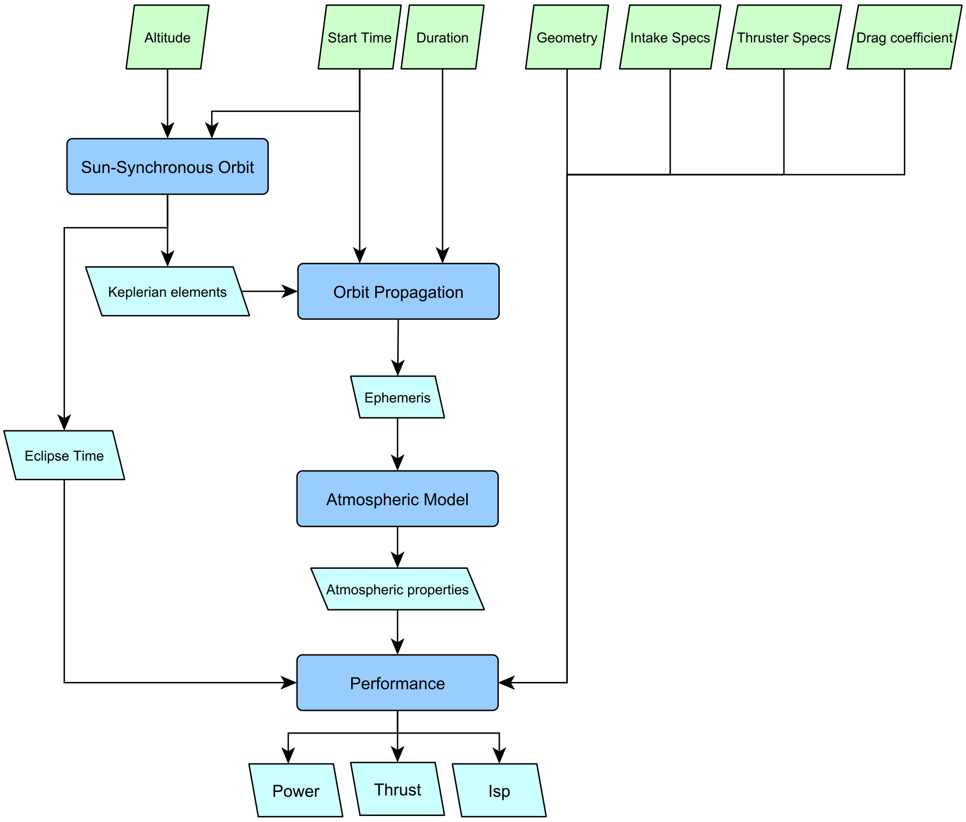

Figure 4.1: Process flowchart. User inputs (green), outputs (cyan) and process (blue).

Given the orbital altitude, the semi-major axis can be calculated as $a = h + a_e$. In a circular orbit, the eccentricity (e) is approximately zero, and the argument of perigee (ω) and true anomaly (υ) are undefined. In this case, the argument of latitude u represents the angle measured between the ascending node vector and the position vector of the spacecraft. This parameter was set to $0°$. The orbital inclination (i) can be obtained by replacing the values in Equation 3.8 and the right ascension of the ascending node (RAAN) is set to be $90°$ at equinoxes and $0°$ at solstices.

The calculated orbital elements are subsequently utilized by the orbit propagator, which is responsible for determining the ephemeris of the spacecraft. By using the orbital elements as input, the orbit propagator calculates and predicts the precise position and velocity of the spacecraft at different points in time. Furthermore, the eclipsed time during the orbital period is also calculated by Equations 3.5 and 3.6 for further power analysis. The following code represents the implementation of the `SSOBlock` function based on provided explanation.

```matlab
function  [SemiMajorAxis,period,eccentricity,ArgLatitude,
   inclination,RAAN,EclipseDuration,IlluminationPercentage]=
   SSOBlock(altitude,StartTime)
    %%contants
    %J2 coefficient
    J2 = 1.08263*10^(-3);
    %Earth radius at the equator
    radius = 6378;
    %gravitational parameter
    mhu = 398600.44;
    %SSO precession rate
    rate = 2*pi()/(365.242199*24*3600);
    %SSO precession rate
    taxa = 360/365.242199;

    %%orbital elements
    SemiMajorAxis = altitude+radius;
    period = 2*pi()*sqrt((SemiMajorAxis^3)/mhu);
    period = period/60;
    eccentricity = 0;
    ArgLatitude = 0;
    inclination = acosd((-2*rate/(3*J2*radius^2*sqrt(mhu)))*
       SemiMajorAxis^(7/2));
    YearAnalysis = year(StartTime);
    reference = datetime(YearAnalysis, 6, 20, 12, 0, 0); %summer
       solestice (0 deg)
    RAAN = (caldays(between(reference, StartTime,'days')))*taxa;

    %%eclipse
    IlluminationPercentage = (pi()+2*acos(radius/(radius+altitude))
       )/(2*pi());
    EclipseDuration = (1-IlluminationPercentage)*period;
end
```

4.2 Orbit propagator block

There are various orbit propagation models available, each designed to cater to the required accuracy of a specific mission. The complexity of these models varies depending on the number of perturbations taken into account. As more factors are considered, the models become more intricate, necessitating higher computational power and time for calculations.

A MATLAB® in-built Orbit Propagator block [43] was used for the purpose. The block contains two propagation methods: "Kepler (unperturbed)" or "numerical (high precision)".

"Kepler (unperturbed)" uses universal variables and Newton-Raphson iteration to propagate spacecraft orbits over time. This analytical algorithm is fast but presents some limitations. This method accounts only for central body spherical gravity (point-mass) and no other perturbations, making it inadequate for propagating SSO.

"Numerical (high precision)" uses a Simulink® solver to integrate position and velocity from central body gravitational acceleration at each simulation time-step. The method for computing central body acceleration depends on the current setting for the parameter "Gravitational potential model":

- "Point-mass" that treats the central body as a point-mass, including only the effects of spherical gravity.
- "Oblate ellipsoid (J_2)" which adds the perturbing effects of the second-degree, zonal harmonic gravity coefficient J_2, accounting for the oblateness of the central body.
- "Spherical harmonics" which increases fidelity by including higher-order perturbation effects accounting for zonal, sectoral, and tesseral harmonics.

As seen in Chapter 2, spacecraft in VLEO are affected by a broad spectrum of perturbations due to Earth's gravity field. Earth's gravitational field is highly irregular due to its uneven mass distribution. Thus, spherical harmonics are mathematical functions defined on the surface of a sphere that are commonly used to model this complex field. These functions help to approximate the non-uniform distribution of Earth's mass, enabling a more accurate representation of the gravitational potential across the globe. Nonetheless, the J_2 perturbation stands out as the most significant perturbation in terms of Earth's non-uniformity, as represented in Figure 2.1.

The present study only considers the J_2 perturbation which is the most relevant when propagating a SSO. Therefore, "numerical propagation" and "oblate ellipsoid J_2" model were selected. Since the main goal of the analysis is to determine the required instantaneous thrust for drag compensation, the effect of atmospheric drag can be neglected. The thrust applied by the propulsion system will counteract the drag, allowing the analysis to focus solely on the task of maintaining the desired orbital altitude which is hindered by Earth's gravity. The remaining perturbations such as gravitational effects of other bodies and solar radiation are neglected in this analysis.

The numerical propagation method uses a solver for solving the ordinary differential equation (ode) 3.7 and getting the position of the spacecraft over time. The optimal solver balances acceptable accuracy with the shortest simulation time. Identifying the optimal solver for a model requires experimentation [44]. Accordingly, a variety of solvers provided by Simulink® were tested.

Firstly, orbit propagation was conducted with different fixed-steps solvers and then compared. As the propagated orbit is circular, the orbital altitude is expected to maintain its altitude. Figure 4.2a exhibits a noticeable pattern of increasing orbital altitude for low-order solvers, suggesting to be inadequate for the study. It was concluded that only solvers with order greater than four (ode4, ode5, ode8) provide the necessary level of precision. Note that increasing the order-level of solvers enhances accuracy at the expense of computational time.

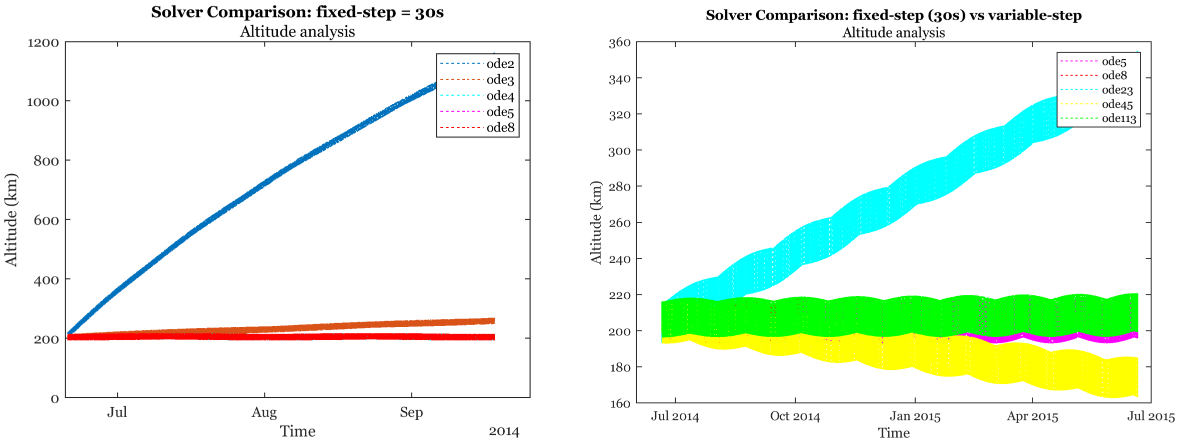

(a) (b)

Figure 4.2: Altitude analysis: fixed-step vs variable-step solvers.

Secondly, orbit propagation using variable-step solvers were also analysed. These solvers adjust their step-size during the simulation to enhance computational efficiency. When a model's states are changing rapidly, they reduce their step-size to increase accuracy. This adaptive approach allows to strike a balance between accuracy and computational efficiency, resulting in faster simulations while ensuring the required level of precision. Figure 4.2b compares the computed altitude using fixed-step and variable-step solvers (ode23, ode45, ode113).

ode23 (Bogacki-Shampine) and ode45 (Dormand-Prince) solvers were found to be inadequate, as they fail to maintain the altitude. Upon careful analysis, it has been concluded that only the ode113 (Adams) solver demonstrates the necessary capabilities for further advancement in this study.

Next, the performance of the successful solvers was subjected to further analysis to quantify the propagation error and ascertain its suitability for the study's objectives. Based on Figure 4.3 and Table 4.1, ode113 can be discarded as it exhibits a significant propagation error when compared to ode8 (Dormand-Prince). Note that ode8 is regarded as the most accurate among the fixed-step solvers due to its highest order. The remaining solvers present insignificant errors. The error was determined by comparing the last position of each solver with the one provided by the ode8 solver.

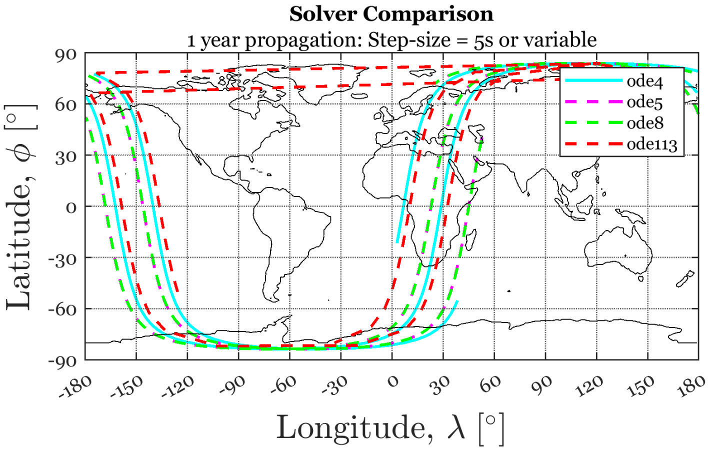

Figure 4.3: Trajectory analysis: different solvers with the same time-step.

Table 4.1: Error quantification analysis: different solvers with the same time-step.

Solver	Time-step (s)	Time (min)	x error (%)	y error (%)	z error (%)
ode4	5	250	0.0604	0.0078	0.0077
ode5		400	0.0012	0.0002	0.0002
ode8		809		ref	
ode113		5	117.9216	185.7206	206.3020

Note the primary objective of this study is to evaluate the spacecraft's drag profile and determine the maximum drag it could encounter. In other words, position accuracy is not the primary concern of this study, instead, it focuses on exploring a wide range of geographic coordinates and environmental conditions to establish the maximum thrust requirement. Consequently, minor errors in terms of position precision are deemed acceptable as the analysis encompasses all potential coordinates, whether they are advanced or delayed in time. Since ode5 (Dormand-Prince) and ode4 (Runge-Kutta) present insignificant errors during one year of propagation and faster time simulations, ode8 may also be discarded as it takes longer to propagate the orbit.

Moreover, a study was conducted using ode5 to explore the impact of different time-steps on simulation time and accuracy. Similarly, decreasing the time-steps enhances accuracy at a cost of computation time. Thus, the simulation of 5 s is considered the most accurate and serves as a baseline for further comparison. From Figures 4.4a, 4.4b and Table 4.2, it is concluded that a time-step of 30 s is satisfactory regarding the associate error and simulation time.

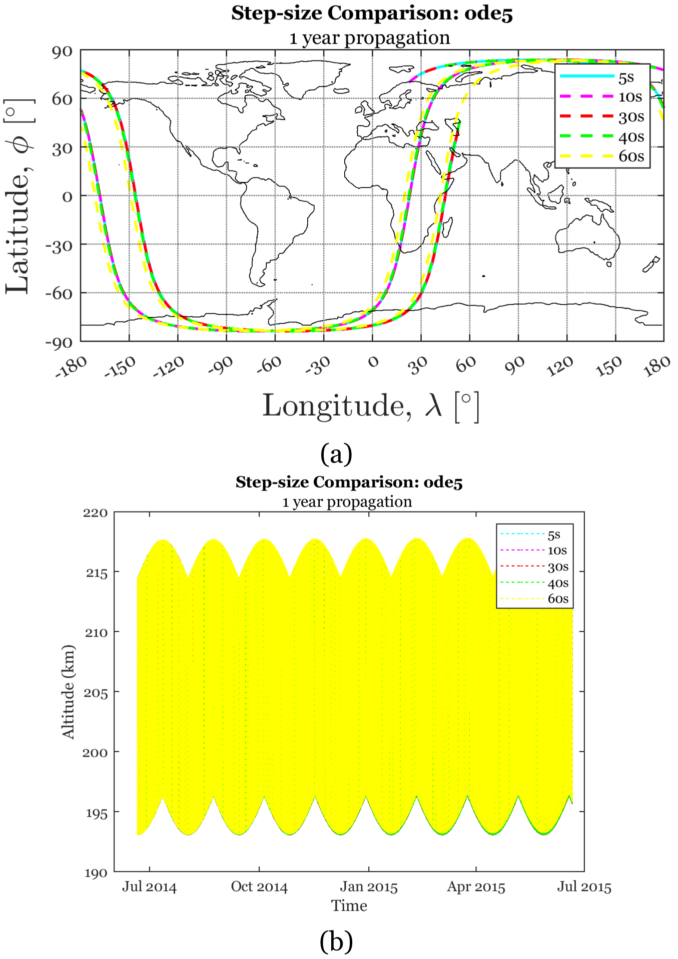

Figure 4.4: (a) Trajectory analysis: ode5 for different time-steps. (b) Altitude analysis: ode5 for different time-steps.

Table 4.2: Error quantification analysis: ode5 for different time-steps.

Time-step	Solver	Time (min)	x error (%)	y error (%)	z error (%)
5	ode5	400	ref		
10		204	0.0370	0.0048	0.0047
30		73	12.4321	1.5194	1.4796
40		63	47.7512	7.0085	4.5848
60		35	257.7308	65.4708	8.7916

Finally, a comparison was made between the ode5 and ode4 solvers using different time-steps, to identify the most efficient simulation that maintain satisfactory accuracy. According to Figure 4.5 and Table 4.3, it was concluded that ode4 solver would require more time to attain a satisfactory level of accuracy in comparison to the ode5 solver when using a time-step of 30 s.

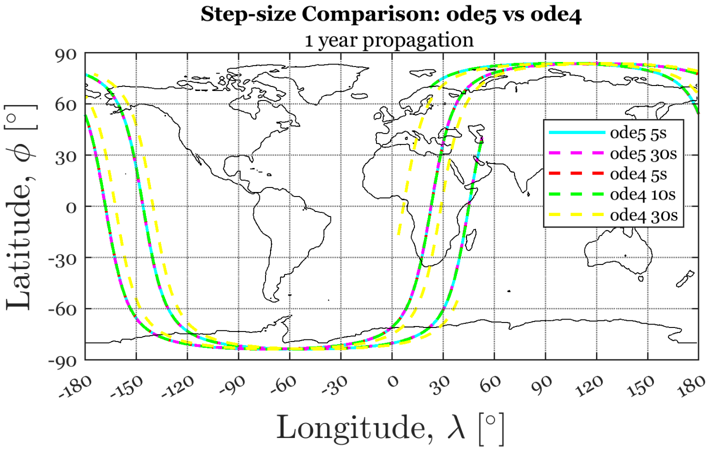

Figure 4.5: Trajectory analysis: ode4 vs ode5 solvers.

Table 4.3: Error quantification analysis: ode4 solver for different time-steps compared to ode5 solver and a time-step of 5 s.

Solver	Time-step (s)	Time (min)	x error (%)	y error (%)	z error (%)
ode4	5	250	0.0616	0.0079	0.0079
	10	125	1.9273	0.2459	0.2490
	30	40	177.2149	69.1725	142.7824

By assessing the performance of each solver, ode5 solver with a time-step of 30 s was deemed as the most adequate solver for numerical orbit propagation. However, the choice of the solver used in the application analysis is left to the user's discretion. The app provides the user with the flexibility to tailor the analysis according to their needs and preferences, ensuring the app's usability and effectiveness for a wide range of applications.

After the simulation, the orbit propagator provides the position and velocity of the spacecraft in Earth-Centered Earth-Fixed (ECEF) frame which is the International Terrestrial Reference Frame (ITRF), represented in Figure 3.9b. The spacecraft's ephemeris will be an input on atmospheric model block which requires a geodetic coordinates frame. This way, the position was transformed into geodetic/geographic coordinates according to the WGS84 model [45]. The following piece of code implements this block, and the algorithm was devised based on the provided explanation.

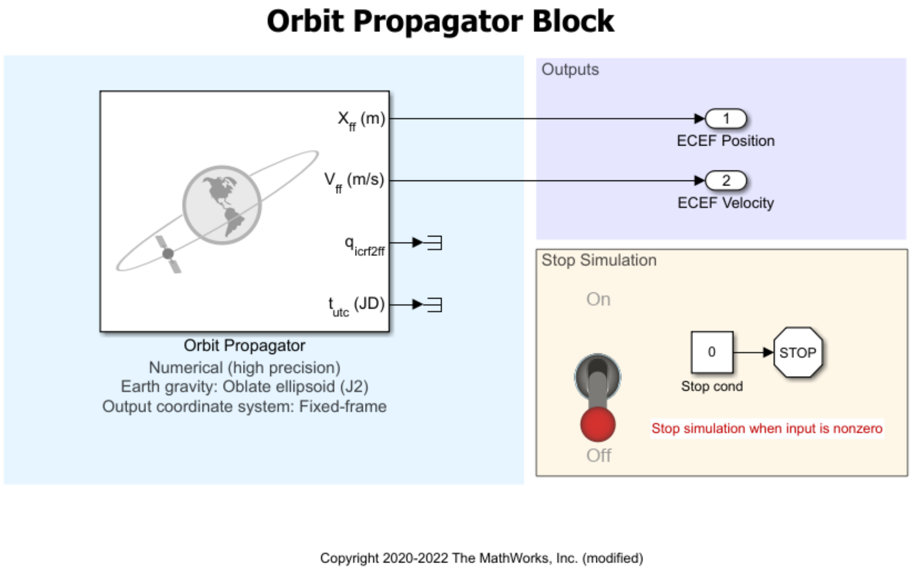

Figure 4.6: Simulink model: Orbit Propagator.

```matlab
function [altitude,latitude,longitude,velocity]= OrbitPropagatorBlock(StartTime,SemiMajorAxis,inclination,RAAN,ArgLatitude,solver,TimeStep,duration)
    %opens Simulink model
    open_system('PropagationModel')
    %propagation parameters
    PropagationMethod = 'Numerical (high precision)';
    GravitationalModel = 'Oblate Ellipsoid (J2)';
    CentralBody = 'Earth';
    OrbitType = 'Circular inclined';
    %configures orbit propagator block
    set_param('PropagationModel/Orbit Propagator', StartTime, PropagationMethod, GravitationalModel, OrbitType, CentralBody, SemiMajorAxis, inclination, RAAN, ArgLatitude);
    %configures numerical method (solver)
    set_param('PropagationModel', solver, TimeStep, duration);
    %simulates Simulink model
    [position_ECEF, velocity_ECEF] = sim("PropagationModel");
    %transforms ECEF to geodetic coordinates
    [altitude, latitude, longitude] = ecef2lla(position_ECEF,'WGS84');end
```

Furthermore, the user has the option to visualize the orbit trajectory and simulation. Figures 4.7a and 4.7b display an example of a ground tracks and scenario output.

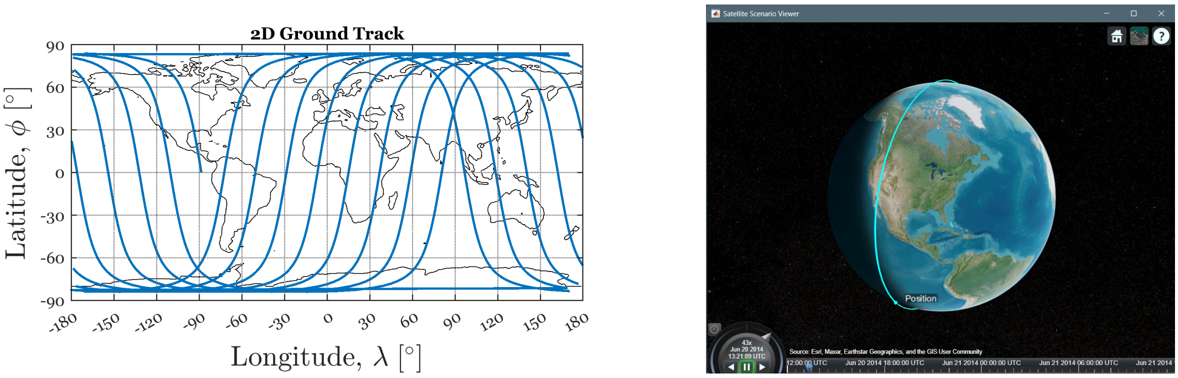

(a) (b)

Figure 4.7: (a) 2D trajectory. (b) 3D representation of the first day of simulation.

4.3 Atmospheric model block

The main task of the atmospheric model block is to access the atmospheric properties the spacecraft will be subjected to during the mission. NRLMSISE-00 atmospheric model [46] was applied for the analysis.

As approached in Chapter 2, atmospheric properties depend on geographic position, solar and geomagnetic activities, and day-night cycles. Thus, NRLMISE-00 calculates atmospheric density and temperature according to orbital altitude, geodetic latitude and longitude, year, day-of-the-year, universal time, and solar and geomagnetic indexes (F10.7 and Ap).

Solar activity inputs require an m-by-1 array that specifies the 81-day average of F10.7 flux (centered on day), an m-by-1 daily F10.7 flux for the previous day, and m-by-7 array of magnetic index information from the current time to 57 h prior. Note that m corresponds to the number of positions being analyzed. *fluxSolarAndGeomagnetic* function [47] extracts the solar flux and geomagnetic data from a MAT-file that is generated by the *aeroReadSpaceWeatherData* function [48]. The space-weather data is provided by CelesTrak® website [6].

This block generates several essential outputs, including the number density of each atmospheric species, the total atmospheric density, and the exospheric and altitude temperatures. The total density assumes particular significance as it serves as a critical input for calculating the drag force experienced by the spacecraft. Moreover, having knowledge of the abundance of each species is of utmost importance, as it determines the composition of the air-breathing mixture that can be ionized to generate thrust. Next, the implementation of this block is presented.

```
function [temperature,density]=AtmosphericModelBlock(year,dayOfYear,UTseconds)
%reads space weather data from the space weather data file downloaded from CelesTrak® and stores the data in a MAT-file
matfile = aeroReadSpaceWeatherData(spaceWeatherFile)

%extracts the solar flux and geomagnetic data from the MAT-file
[f107average,f107daily,magneticIndex] = fluxSolarAndGeomagnetic(year,dayOfYear,UTseconds,matFile)

%calculates atmospheric properties
[temperature, density] = atmosnrlmsise00(altitude,latitude,longitude,year,dayOfYear,UTseconds,F107Average,F107Daily,magneticIndex)
end
```

4.4 Performance block

Finally, the last block of the process is responsible for calculating the required performance for orbit keeping. To maintain the altitude h at a constant level, the thrust T provided by the ABEP system must compensate for the instantaneous drag force F_D:

$$T = F_D = \frac{1}{2}\rho C_D A_f v^2 \quad (4.1)$$

F_D is directly influenced by $\rho(h)$, $v(h)$, and A_f. Note that a constant C_D is considered and the simulation calculates the drag for a frontal flat wall and does not consider an intake shape that induces less drag. At lower altitudes, the ρ and v are higher, leading to more significant drag effects. Additionally, larger A_f encounter more resistance from the atmosphere, resulting in higher F_D. The available mass flow rate $\dot{m}$ for the thruster can be calculated via:

$$\dot{m} = \eta_c \rho A_{in} v \quad (4.2)$$

$\dot{m}$ at the inlet of the thruster will depend on η_c, intake area A_{in}, and orbital altitude ($\rho(h)$ and $v(h)$). Based on this equation, an increase in η_c and A_{in}, and a decrease in altitude all lead to an enhancement in $\dot{m}$, thereby enabling a higher achievable T. The provided T by the propulsion system is also expressed by:

$$T = \dot{m} v_e \quad (4.3)$$

By inserting this expression in Equation 4.1:

$$\dot{m} v_e = \frac{1}{2} \rho C_D A_f v^2 \quad (4.4)$$

This equation can be rearranged for the required specific impulse I_{sp} according to:

$$I_{\text{sp}} = \frac{v_e}{g_0} = \frac{C_D v}{2\eta_c g_0} \frac{A_f}{A_{in}} \approx \frac{C_D v}{2\eta_c g_0} \quad (4.5)$$

For this analysis, $\frac{A_f}{A_{in}}$ is assumed to be approximately 1. Since the orbit is circular, v remains nearly constant. Consequently, the mean velocity value was assumed and v_e and I_{sp} resulted in nearly constant values. Here, I_{sp} depends on altitude and η_c. As expected, increasing η_c reduces the required I_{sp} to achieve the same jet momentum since more air is collected. The required electric power P_{in} is calculated by:

$$P_{in} = \frac{T v_e}{2\eta_t} = \frac{\dot{m} v_e^2}{2\eta_t} = \frac{\rho A_{in} C_D^2 v^3}{8\eta_c \eta_t} \quad (4.6)$$

Similarly, the more efficient the thruster and the collector, the less P_{in} is demanded to generate T. Additionally, lower orbits and larger spacecraft require more power for drag compensation. A first approach for the required solar arrays area A_{SA} can be calculated by:

$$A_{SA} = \frac{P_{in} \zeta}{a_p \eta_{as}} \times (2 - \frac{t_{sunlight}}{T}) \quad (4.7)$$

where $\zeta = 1.2$ is a margin to account for sub-systems other than the thruster and $\eta_{as} = 0.9$ is included to account for losses resulting from the assembly of multiple solar panels into larger sections [12]. The necessary A_{SA} is oversized to ensure sufficient power supply during the periods in which the spacecraft is in the shadow and not receiving sunlight for power generation. This analysis assumes that the solar panels are constantly oriented perpendicular to the sun and do not experience degradation, acknowledging that this assumption is not entirely realistic but serves as an initial estimation. The last block which aims to evaluate the required performance was developed under the represented equations. Next, a piece of code is presented.

```
  function [drag,AvailableMassFlow,ExhaustVelocity,power,SolarArea]=PerformanceBlock(density,DragCoefficient,velocity,FrontalArea,CollectorEfficiency,ThrusterEfficiency,IlluminationPercentage)

     drag = 0.5*density*DragCoefficient*mean(velocity)^2*FrontalArea;
     AvailableMassFlow = CollectorEfficiency*density*mean(velocity)*FrontalArea;
     ExhaustVelocity = mean(velocity)*DragCoefficient/(2 CollectorEfficiency);
     SpecificImpulse = ExhaustVelocity/9.81;
     power = AvailableMassFlow*ExhaustVelocity^2/(2*ThrusterEfficiency);
     SpecificPower = 368;
     margin = 1.2;
     AssemblyEfficiency = 0.9;
     SolarArea = max(power)*(1+1-IlluminationPercentage)*margin/(SpecificPower*AssemblyEfficiency);
end
```

The final design of the application is represented in the following Figure 4.8.

MATLAB App

Inputs

Altitude (km): 250
Start Time: 2009-09-01 12:00:00
Duration (years): 2
Frontal Area (m^2): 1.1
Drag coefficient: 3.7
Thruster efficiency: 0.35
Collector efficiency: 0.3

Simulation parameters

Solver: ode5
Step (s): 30

Outputs

☐ Display 2D trajectory
☐ Display scenario
☑ Save outputs
File prefixe: Goce

Ready! New simulation?

Analysis

Sun-Synchronous-Orbit (SSO)

Inclination (deg): 96.50
Period (min): 89.50
Eclipsed period (%): 41.23
Mean Velocity (km/s): 7.82

Atmospheric properties

Temperature (K): 799.44
Total Density (kg/m^3): 3.553e-11
O_2 (m^{-3}): 1.282e+13
N_2 (m^{-3}): 2.690e+14
O (m^{-3}): 8.315e+14
Available Mass Flow (kg/s): 3.24e-08

Performance

Figure 4.8: Graphic user interface of the developed MATLAB® app.

4.5 App validation

To validate the data generated by the app, a real mission was replicated and its outputs were compared with reported flight data. GOCE mission was chosen for this validation process due to its operation in very-low altitudes. The flight data of the first 22 months of this mission is reported in [49].

Given that the application was designed to calculate the required performance (thrust and power) for an air-breathing thruster and GOCE spacecraft was equipped with traditional ion engines and stored propellant, a direct comparison of power demand with reported data is not feasible. It is expected that air-breathing engines require more power to generate thrust as their thruster efficiency is inferior. Nevertheless, it is possible to validate aspects such as orbit propagation and environmental characterization by comparing the experienced drag/thrust demands.

4.5.1 Background and flight data

Recently, ESA's GOCE mission was dedicated to mapping Earth's gravity field with exceptional precision to provide the most accurate model of the geoid with an accuracy of $1-2$ cm at a spatial resolution of $110\,\mathrm{km}$. This remarkable level of precision and accuracy was achieved through operation in very-low orbits. The primary role of the spacecraft's propulsion system was to counteract the drag experienced while orbiting. As a result, the spacecraft only experienced acceleration due to gravity. This unique condition allowed a sensitive gradiometer to accurately probe higher-order harmonics of the Earth's gravitational field. The study concluded the gravitational acceleration at Earth's surface is about $9.8\,\mathrm{m/s^2}$, varying from a minimum of $9.788\,\mathrm{m/s^2}$ at the equator to a maximum of $9.838\,\mathrm{m/s^2}$ at the poles due to Earth's oblateness.

The spacecraft, depicted in Figure 3.1a, had the following physical characteristics: a launch mass of $1050\,\mathrm{kg}$, a length of $5.3\,\mathrm{m}$, and a cross-sectional area of $1.1\,\mathrm{m^2}$. Operating at altitudes ranging from $240-260$ km in a polar SSO, the spacecraft utilized two QinetiQ T5 Kaufman-type ion thrusters, which employed Xe propellant and provided a variable thrust within the range of $1.5-20$ mN. This thruster has been designed for a nominal thrust of $0.6-20.6$ mN. The solar arrays delivered $1.6\,\mathrm{kW}$ of end-of-life (EOL) electric power, while lithium-ion batteries were employed to ensure continuous power supply during eclipses [50].

Launched in March 2009 and after depleting its propellant reserves ($40\,\mathrm{kg}$ of Xe) in November 2013, the spacecraft's started deorbiting leading to an uncontrolled re-entry into the atmosphere. As a result, the spacecraft's total operational lifetime spanned 56 months [51],

[49]. This example effectively illustrates how propellant depletion becomes a limiting factor for orbiting in VLEO.

Figure 4.9 represents the thrust history provided by the propulsive system for drag compensation at $\approx 260\,\mathrm{km}$. The majority of the thrust error occurs within $\pm 5\%$ of the thrust demands. This data represents the actual in-orbit thrust demand required to compensate for drag and will be compared to the thrust demand generated by the application. The power demand as a function of the provided thrust by the thruster during the commissioning phase is represented in Figure 4.10.

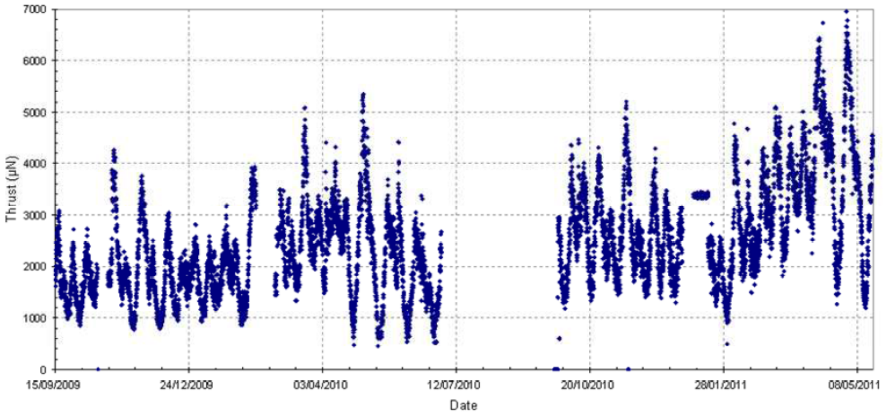

Figure 4.9: Flight data: thrust profile throughout the mission for drag compensation [49].

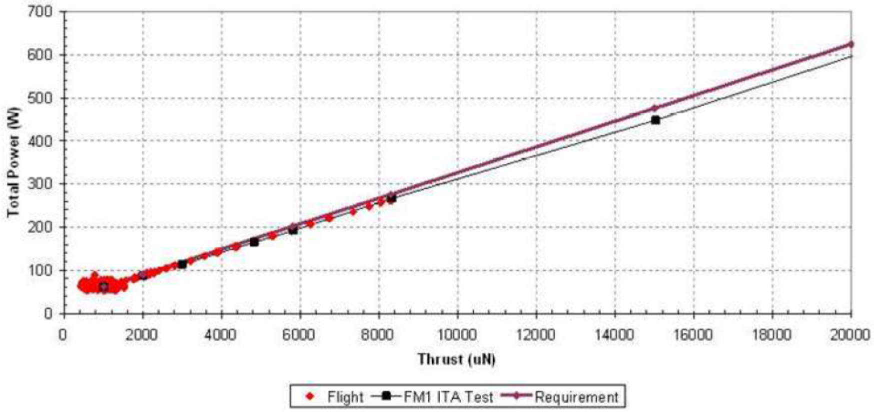

Figure 4.10: Fligh data: Power demand as a function of thrust [49].

The baseline 22-month science mission commenced in September 2009, during which drag-free control operations were continuously conducted at $\approx 259.4\,\mathrm{km}$. There was a brief exception in February/March 2010 when the thruster performance was operated manually. In July 2010, the altitude was raised to $263\,\mathrm{km}$ and the thruster operated at a constant $2.5\,\mathrm{mN}$ through manual commanding after a serious communication malfunctioning. In September 2010, the altitude was gradually lowered to $259.4\,\mathrm{km}$. The orbital inclination was 96.5°, period was ≈90 min and the eclipses up to 37 min. The main flow rate supplied to the thruster varied between $0.087 - 0.531$ mg s^{-1} according to the demanded thrust level [49].

4.5.2 Validation

The mission parameters introduced in the app, which replicate GOCE mission, are presented in Table 4.4.

Table 4.4: App validation: GOCE mission parameters.

Mission	Altitude, h	260 km
	Starting date	1st of September 2009
	Ending date	1st September 2011
Spacecraft	Frontal area, A_f	$1.1\,\mathrm{m}^2$
Environment	Drag coefficient, C_D	3.7
Simulation	Solver	ode5
	Time-step	30 s

The calculated orbit inclination was $96.5°$, period of 89.7 min, and eclipsed period up to 41.1 min. Orbital inclination and period were found to be consistent with the GOCE's provided data. However, the calculated eclipsed period appears to be slightly higher than the reported one. This increase was anticipated because Equation 3.6 assumes the penumbra condition as part of the umbra condition, leading to longer eclipsed periods. Nonetheless, the computed eclipse duration is considered a good approximation for the app main goal.

The resulting experienced drag is depicted in Figures 4.11 and 4.12. According to the results, the experienced drag or thrust demand was predominantly ≈3 mN and within a range of $1.1 - 8.8$ mN. Note that the reported drag was predominantly $2 - 3$ mN and reached as high as 7 mN.

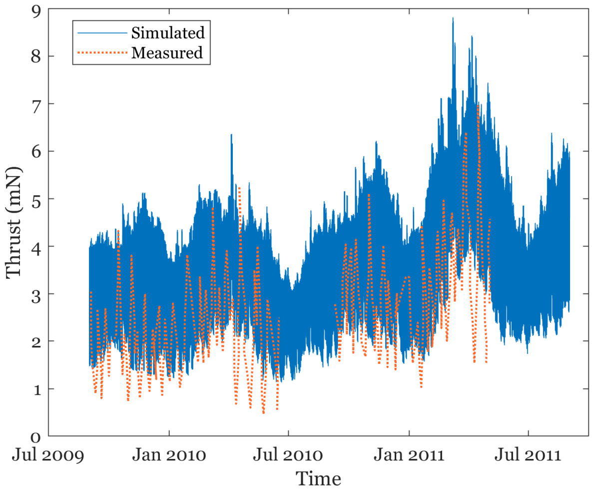

Figure 4.11: App results: Thrust profile throughout the mission.

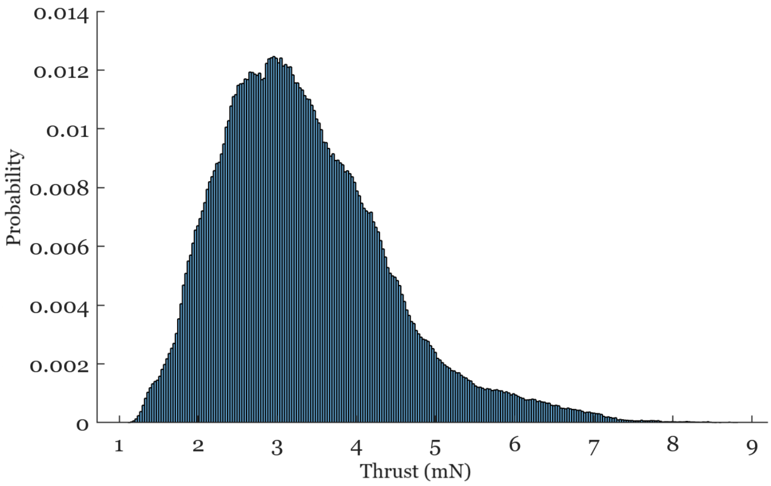

Figure 4.12: App results: Thrust histogram throughout the mission.

The overestimation of the experienced drag can be attributed to two main factors. The first one is the use of atmospheric models, which tend to slightly overestimate atmospheric density within $\pm 5\%$ with respect to actual density [17]. As mentioned in Chapter 2, the dynamic and unpredictable behavior of the thermosphere poses challenges for its modeling. The second one is the assumption of a constant drag coefficient, specifically $C_D = 3.7$ which was the highest measured during the mission. This assumption can lead to an overestimation of drag in certain conditions when the drag coefficient was lower than this value. However, the computed results are considered satisfactory and representative of reality. Consequently, the outputs and applicability of the app were validated.

Chapter 5

Case-study

In this chapter, the feasibility of employing an air-breathing electric engine on a mission similar to GOCE's is examined using the developed app. For this analysis, a spacecraft geometry (A_f) and a orbit (SSO) similar to GOCE's were chosen, but within the feasible range of altitudes for air-breathing technology. The mission parameters entered into the app are outlined in Table 5.1.

The chosen target altitude was $250\,\mathrm{km}$ based on the recognition that air-breathing technology is solely competitive for altitudes beneath $250\,\mathrm{km}$, as previously identified. This is mainly due to the extremely sparse atmospheric density at higher altitudes that makes plasma ignition for thrust generation unattainable.

Table 5.1: Feasibility study parameters: GOCE at $250\,\mathrm{km}$.

Mission	Altitude, h Starting date Ending date	$250\,\mathrm{km}$ 1st of September 2009 1st September 2011
Spacecraft	Frontal area, A_f	$1.1\,\mathrm{m}^2$
Environment	Drag coefficient, C_D	3.7
ABEP system	Collector efficiency, η_c Thruster efficiency, η_t	0.3 0.35
Simulation	Solver Time-step	ode5 $30\,\mathrm{s}$

To account for the omission of drag contribution from parallel surfaces, a $C_D = 3.7$ was utilized in the analysis. Also, collector and thruster efficiencies were selected in alignment with SoA ABEP systems. Lastly, the numerical orbit propagation was executed using the ode5 solver with a time-step of $30\,\mathrm{s}$, as it emerged as the optimal solution in terms of computational efficiency according to app's performance objectives.

Hereby, the outputs of the app for the given mission parameters are presented. The calculated orbital inclination was $96.5°$, period of $89.5\,\mathrm{min}$, and eclipsed period up to $41.23\,\mathrm{min}$. As expected, the computed orbital period starts to decrease as orbital altitude decreases due to the increase in orbital velocity ($89.5 < 89.7\,\mathrm{min}$). Conversely, the computed eclipsed period starts to increase as orbital altitude decreases since lower orbits are prone to longer eclipses ($41.23 > 41.1\,\mathrm{min}$).

The resulting thrust histogram, which corresponds to the experienced drag throughout the mission, is depicted in Figure 5.1. According to the results, the engine must be able to operate predominantly ≈ 4 mN and within a range of $1.6 - 11.5$ mN. Decreasing the altitude resulted in an increase in experienced drag and, consequently, thrust and power demands.

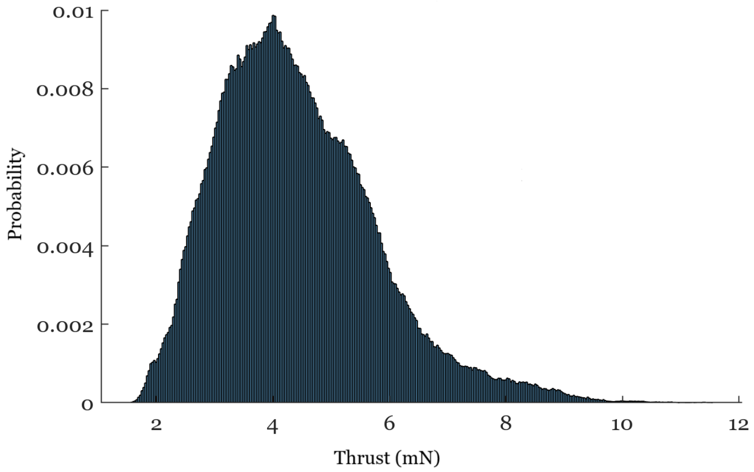

Figure 5.1: Thrust demand histogram throughout the mission.

Upon initial observation of Figure 5.2a, a discernible increasing trend in thrust demand is evident. The observed trend arises from the progressive increase of solar activity leading up to a peak in 2014 (Figure 2.3a). On the other hand, short-term variations are induced by fluctuations in atmospheric density, which depend on seasonality, time of day, and geography.

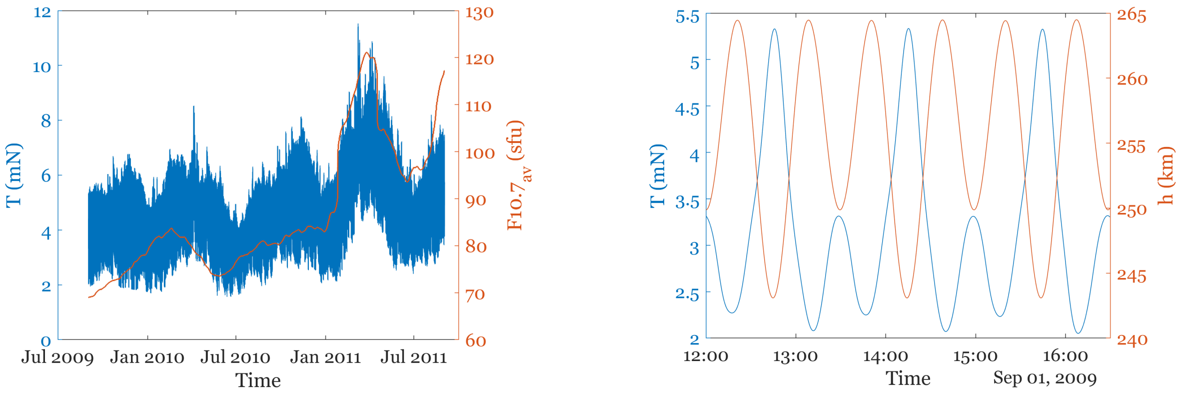

(a)

(b)

Figure 5.2: (a) Thrust and solar activity profiles. (b) Thrust and ellipsoidal height profiles.

The relationship between thrust and altitude profiles was also verified and displayed in Figure 5.2b. Although the altitude remains approximately constant throughout the mission, there are minor oscillations due to Earth's oblateness. Higher altitudes experience lower atmospheric density and, consequently, lower thrust demand. The solar heating's effect on atmospheric density is also observable in this figure. The simulated orbit is a dawn-dusk SSO, i.e., the local mean solar time of passage for equatorial latitudes is around sunrise or sunset as represented in Figure 5.3. The effects of atmospheric heating become evident through the disparities observed between the ascending and descending nodes. The atmospheric density increases while descending due to solar heating during the day and, conversely, decreases while ascending due to cooling during the night.

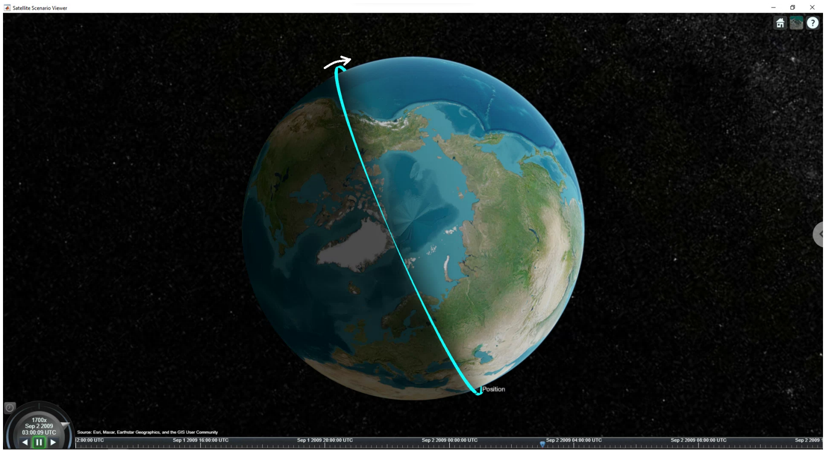

Figure 5.3: Sun-synchronous dawn-dusk orbit scenario (seen from the north pole),

Figure 5.4 illustrates the simulated power demand throughout the mission. The propulsive system predominantly requires $\approx 280\,\mathrm{W}$ within a range of $107.5 - 793.9\ \mathrm{W}$. Indeed, the calculated values are higher than the reported from GOCE at $260\,\mathrm{km}$ ($\approx 100\,\mathrm{W}$) due to three primary factors. Firstly, the simulated lower altitude leads to higher thrust demands and, hence, power requirements. Secondly, the ABET efficiency is comparatively lower than that of traditional electric thrusters due to the inferior performance of atmospheric propellants, requiring more electric energy to generate thrust. Furthermore, the available mass flow for the thruster is in the range of $0.0324 - 0.2392\ \mathrm{mg\,s^{-1}}$, which is considerably lower than the provided to GOCE's thruster ($0.087 - 0.531\ \mathrm{mg\,s^{-1}}$). Thirdly, the longer eclipse also contributes to this increment to ensure that there is stored solar power during eclipses. It is important to emphasize that the calculated power only considers the thruster demands and does not account for all other electrical systems on the spacecraft.

To meet the power requirements, at least $4\,\mathrm{m}^2$ of solar arrays are necessary. This value already incorporates a margin of 1.2 for other electrical systems than the thruster. This required solar array area calculation assumes that solar panels are always perpendicular to solar radiation, which is not accurate. In reality, the orientation of the solar panels changes as the spacecraft orbits the Earth. Therefore, a more comprehensive analysis that accounts for the varying angles of solar radiation should be considered to accurately determine the required solar arrays area. The calculated value is a first estimate.

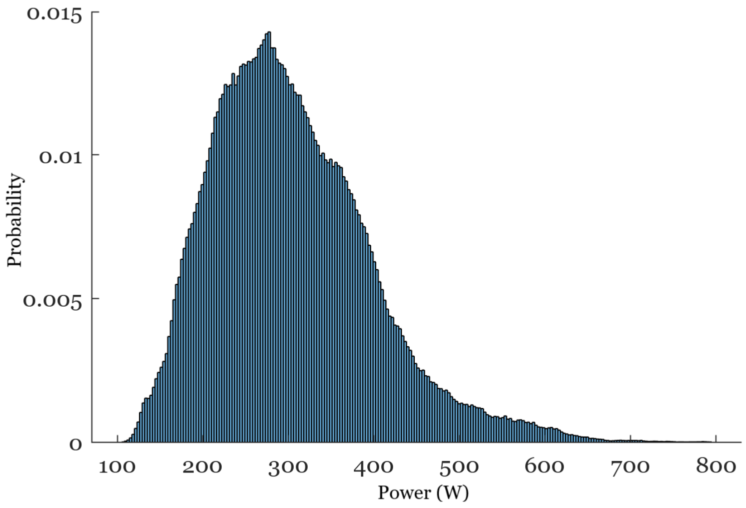

Figure 5.4: Power demand histogram throughout the mission.

In conclusion, the ABEP system ($\eta_t = 0.35$ and $\eta_c = 0.3$) achieves a $I_{\text{sp}} \approx 4913.6$ s, an $v_e \approx 48.2$ km/s and a $T/P_{in} \approx 14.52\,\text{mN/kW}$ which are values within the SoA experimental tests. As reported, the solar arrays furnished $1.6\,\text{kW}$ of electric power to the GOCE spacecraft, signifying a key constraint on its operation. Based on the results, operating at $250\,\text{km}$ necessitates a peak power of $793.9\,\text{W}$, which is within the available electrical supply. This implies that the available power is sufficient to support thruster operation at this altitude.

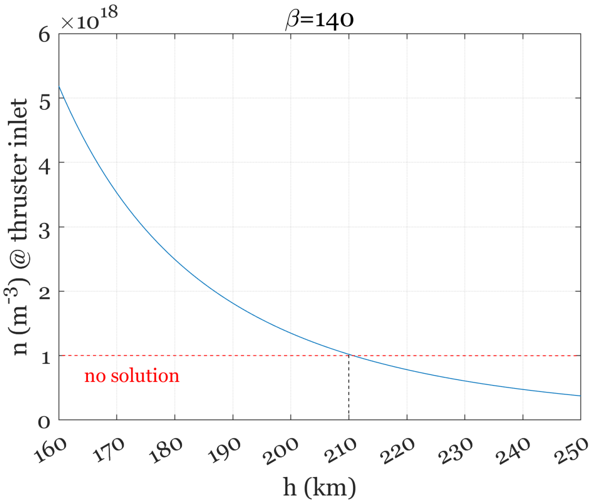

Figure 5.5: Atmospheric number density at the thruster inlet considering SoA intakes performance ($\beta = 140$).

However, the minimum required number density for thruster operation ($n \geq 10^{18}\ \text{m}^{-3}$) is only achievable for altitudes lower than $210\,\text{km}$, considering a compression factor of $\beta = 140$, as depicted in Figure 5.5. This condition turns the mission unfeasible for altitudes exceeding $210\,\text{km}$, unless there are advancements in intake system technology. In other words, a mission with a spacecraft like GOCE's is not feasible at $250\,\mathrm{km}$ using an ABEP system for thrust generation due to intake's inability to sufficiently compress the surrounding atmosphere for plasma generation at current level of development.

To delve further into the analysis of this mission's feasibility with an ABEP system, additional orbital altitudes with the same thruster were studied. The study focused on the most critical condition during the mission (on 8^{th} of March of 2011), when the highest thrust demand occurred, to ensure drag compensation. Given the established understanding that thruster operation is not feasible at altitudes higher than $210\,\mathrm{km}$, these higher altitudes can be eliminated from consideration. Figure 5.6 shows the thrust and power demands are $27.04\,\mathrm{mN}$ and $1.85\,\mathrm{kW}$ at $210\,\mathrm{km}$. Here, the demanded power already exceeds the supplied ($1.85 > 1.6$ kW), requiring more solar arrays than available which could introduce more drag. This renders the mission unfeasible at all altitudes since the power demand rises for lower altitudes. It is worth noting that the GOCE spacecraft employs body-mounted solar arrays along with solar panels on its wings to minimize drag. In summary, a spacecraft with the characteristics of GOCE can not currently operate using air-breathing technology.

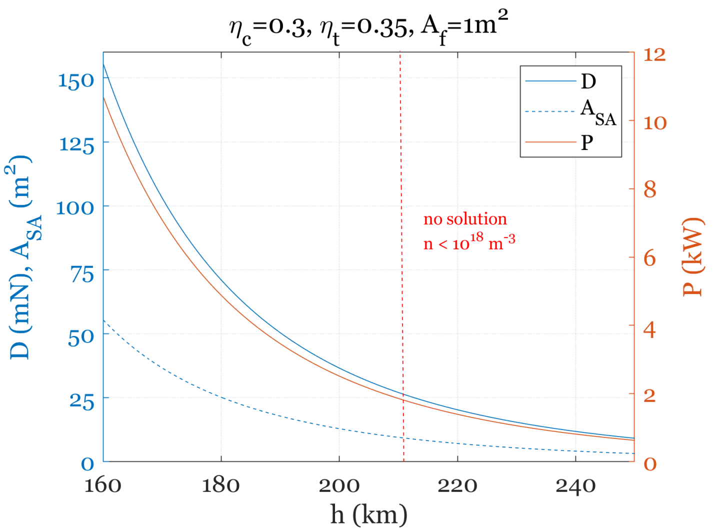

Figure 5.6: Impact of different very-low altitudes on the required performance.

Nonetheless, the potential for such a mission could be enhanced through advancements in intake and thruster performance. The elevation of the compression factor could facilitate operations at higher altitudes than $210\,\mathrm{km}$ where the necessary power is accessible. Moreover, improvements in thruster and collection efficiencies would also reduce power demands, as depicted in Figures 5.7a and 5.7b, possibly enabling operations at $210\,\mathrm{km}$ or even lower.

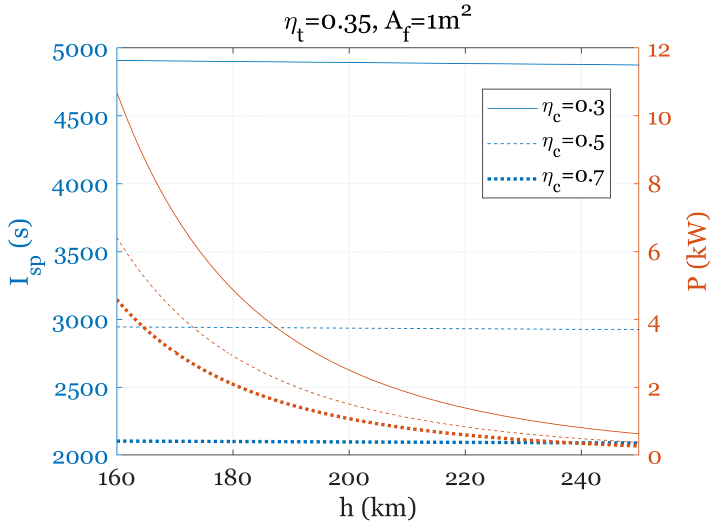

(a) Required performance for different collection efficiencies.

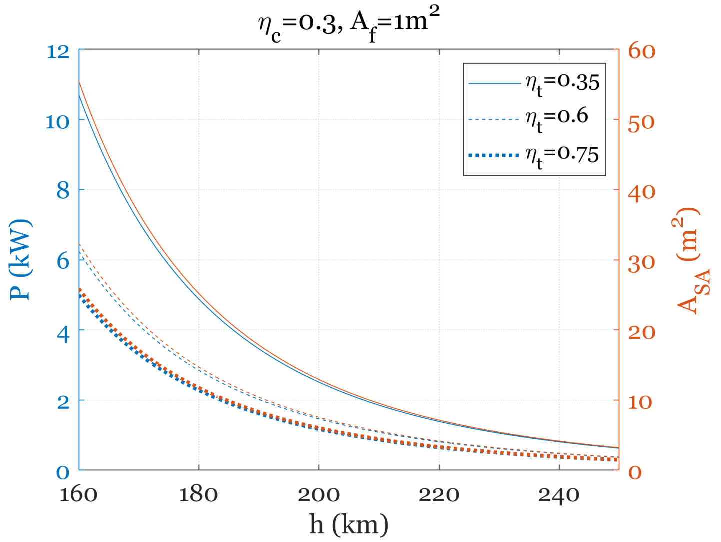

(b) Required performance for different thruster efficiencies.

Figure 5.7: Impact of technological advancements on the required performance.

Figure 5.7a illustrates that an increase in η_c leads to a reduction in the required I_{sp} and P_{in}, thereby facilitating operations at lower orbital altitudes as T/P_{in} is increased. Increasing η_c to 0.5 leads to a decrease in power demand to $1.11\,\text{kW}$ operating at $210\,\text{km}$. In turn, increasing η_c to 0.7 requires $0.79\,\text{kW}$. Also, a higher η_c reduces the required I_{sp} due to higher achieved mass flow. These enhancements would indeed enable the successful execution of the mission. Fixing η_t to 0.35 and increasing the η_c to 0.5 would enable GOCE mission within $198 - 210$ km, considering the available power. In turn, increasing η_c to 0.7 would lower the minimum altitude to $188\,\text{km}$.

Figure 5.7b demonstrates that an increment in η_t decreases the power demand, hence, the required solar arrays area. An increment in η_t to 0.6 leads to a decrease in power demand to $1.08\,\mathrm{kW}$ and solar array area to $5.56\,\mathrm{m}^2$ operating at $210\,\mathrm{km}$. In turn, increasing η_t to 0.75 requires $0.86\,\mathrm{kW}$ and solar array area of $4.45\,\mathrm{m}^2$. Similarly, increasing η_t would enhance the feasibility of the mission, as the same thrust could be generated using less power through increased thruster efficiency. Fixing η_c to 0.3 and increasing the η_t to 0.6 would enable the mission within $197 - 210$ km, considering the available power. In turn, increasing η_t to 0.75 would lower the minimum altitude to $190\,\mathrm{km}$. Overall, it can be inferred that further advancements in ABEP systems are imperative to facilitate missions involving spacecraft of dimensions similar to that of GOCE.

To finalize, spacecraft with smaller frontal areas were also subjected to analysis, given that the frontal area significantly contributes to the experienced drag. Figure 5.8 assesses the operation with different cross-sectional areas. As expected, smaller cross-sectional areas require less thrust and power demands as the experienced drag is reduced. A standard spacecraft like GOCE, experiences a drag of $27.04\,\mathrm{mN}$ and requires $1.85\,\mathrm{kW}$ to operate at $210\,\mathrm{km}$. At the same altitude, a small-satellite experiences $8.11\,\mathrm{mN}$ and requires $0.55\,\mathrm{kW}$ and $2.86\,\mathrm{m}^2$ of solar arrays. Finally, a cubesat experiences even less drag $0.27\,\mathrm{mN}$ and demands $20\,\mathrm{W}$ and $0.1\,\mathrm{m}^2$ of solar arrays.

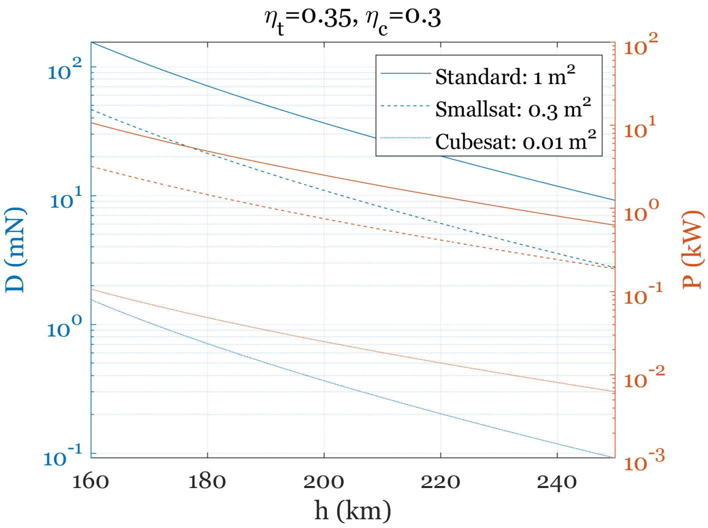

Figure 5.8: Impact of different cross-sectional areas on required performance.

From the results, it can be concluded that reducing spacecraft area can also enable operations with current air-breathing engines. However, the miniaturization of spacecraft also poses some challenges to electric propulsion such as limited space and power generation. Small satellites have space constraints, making it challenging to fit propulsion systems and generate power due to their small surface area for solar panels. Despite these challenges, the miniaturization trend in the space industry is pushing the boundaries of what is possible with small satellites. For example, the gridded ion thruster NPT30-I2-1U developed by ThrustMe company is already fully proven with iodine as the propellant and can provide $0.3 - 1.1$ mN at $35 - 65$ W [52]. It comes in 1U and 1.5U sizes. Also, ExoMG is a miniaturized Hall-effect thruster developed by Exotrail to operate with xenon that can provide more than 2 mN at 53 W of discharge [53]. It is important to emphasize that the available space also imposes limitations on the size of intake inlet area, constraining atmospheric collection performance.

In conclusion, the progression of air-breathing electric propulsion systems is imperative to enable missions involving spacecraft dimensions like GOCE's. It is noteworthy that smaller spacecraft are more likely to be effectively operated using state-of-the-art air-breathing engines.

Chapter 6

Conclusion

As previously discussed, very-low orbits offer numerous advantages for remote sensing missions. However, operating in this region is challenging due to the increased atmospheric density. Traditional space propulsion systems, reliant on onboard propellants to counteract drag and maintain orbital altitude, are unable to sustain extended missions as they rapidly deplete their propellant reserves due to the significant drag. In response to this challenge, air-breathing electric propulsion technology has emerged as a promising solution for enabling near-Earth orbits. ABEP represents an innovative approach that utilizes residual atmospheric particles to generate thrust without the need to carry conventional propellants onboard. From the literature review, state-of-the-art ABEP systems offer approximately thruster efficiencies of 0.35, intake efficiencies of 0.3, and intake compression ratios of 140.

The primary objective of this thesis was to create an app capable of identifying the requirements for maintaining a spacecraft's orbit in VLEO to further assess the feasibility of using state-of-the-art ABEP technology for this purpose. The app was designed to propagate the orbit, characterize the very-low environment, and determine operational prerequisites, such as thrust and power requirements, based on user-specified mission parameters. The app also provides outputs such as required solar array area, specific impulse, Keplerian orbital elements, and atmospheric properties along the mission. The app is tailored to consider sun-synchronous orbits as they were identified as the most suitable for ABEP operations. To facilitate these complex numerical calculations, the app was developed using MATLAB®.

GOCE mission, which operated in very-low altitudes, was selected to be replicated within the app to validate its outputs by comparing them with the reported flight data. The outcomes of the app offered valuable insights into the feasibility of conducting very-low missions with air-breathing technology, and guidelines for future development.

In the case-study, the feasibility of employing ABEP on a spacecraft like GOCE's at $250\ \mathrm{km}$ was analyzed with the developed app. The analysis showed that current ABEP is not yet capable of effectively propelling a mission under these conditions. The primary limitation identified was the poor performance of the intake compression, which could not provide the thruster with the required atmospheric number density for ignition ($n \geq 10^{18}\ \mathrm{m}^{-3}$). SoA intake systems can achieve a compression factor of approximately 140, limiting ABEP operation to altitudes lower than $210\,\mathrm{km}$. However, it is important to note that the required power for the mission could be achieved within the constraints of the spacecraft's power supply ($1.6\,\mathrm{kW}$). The critical factor identified here was the intake technology, which requires further development to enable this mission.

Further analysis found that at an altitude of $210\,\mathrm{km}$, the required power for the mission already exceeded the available power supply. In this scenario, while the thruster operation was ensured by atmospheric compression, it was limited by the available power to generate thrust. As lower altitudes were shown to experience greater drag forces, leading to higher power demands, it was concluded that propelling a spacecraft like GOCE's is currently not feasible with the existing ABEP systems at any very-low altitude.

Nonetheless, advancements in intake and thruster performances could enhance the mission. For example, the compression factor improvement could facilitate operations at higher altitudes than $210\,\mathrm{km}$ where the necessary power was accessible. Moreover, improvements in thruster and collection efficiencies would also reduce power demands. Fixing the thruster efficiency to 0.35 and raising the collection efficiency to 0.5 would enable the mission within $198-210\,\mathrm{km}$. On the other hand, fixing the collection efficiency to 0.3 and raising the thruster efficiency to 0.6 would enable the mission within $197-210$ km. Superior performance would enable orbiting at even lower altitudes.

Lastly, spacecraft with smaller frontal areas (< 1.1 m^2) were also subjected to analysis, given that this parameter significantly contributes to the experienced drag. As expected, reducing spacecraft area could also facilitate operations with current air-breathing engines as power demands were reduced. However, the miniaturization of spacecraft also poses some challenges to electric propulsion such as limited space and power generation.

In conclusion, the goals of the thesis were successfully achieved. The developed app demonstrated the capability to simulate real orbit conditions and calculate the required operational performance based on air-breathing thruster specifications. Additionally, the app proved to be a valuable tool for assessing the feasibility of missions with this technology and provided valuable guidelines for its future development.

However, some assumptions were taken to facilitate the numerical calculation required for the study. Further investigation should explore variables such as the varying orientation of solar arrays' surface to the Sun vector and their degradation over time. Furthermore, there is potential for improvement in the calculation of experienced drag, especially in accounting for the actual shape of an air-breathing spacecraft, which would involve considering the shape of the intake rather than relying on a simplistic front wall approximation. Additionally, it might be worthwhile to estimate the drag coefficient throughout an entire mission for more accuracy.

Bibliography

[1] N. H. Crisp, P. C. Roberts, F. Romano, K. Smith, V. Oiko, V. Sulliotti-Linner, V. Hanessian, G. Herdrich, D. García-Almiñana, D. Kataria *et al.*, "System modelling of very low earth orbit satellites for earth observation," *Acta Astronautica*, vol. 187, pp. 475–491, 2021. 1, 13, 15

[2] T. Andreussi, E. Ferrato, and V. Giannetti, "A review of air-breathing electric propulsion: from mission studies to technology verification," *Journal of Electric Propulsion*, vol. 1, no. 1, p. 31, 2022. 1, 5, 6, 23, 24

[3] J. Wu, P. Zheng, Y. Zhang, and H. Tang, "Recent development of intake devices for atmosphere-breathing electric propulsion system," *Progress in Aerospace Sciences*, vol. 133, p. 100848, 2022. xv, xvii, 2, 11, 23, 24, 25

[4] J. V. Llop, P. Roberts, Z. Hao, L. R. Tomas, and V. Beauplet, "Very low earth orbit mission concepts for earth observation: Benefits and challenges," in *Reinventing Space Conference*, 2014, pp. 18–21. xv, 5, 6

[5] P. Crandall and R. E. Wirz, "Air-breathing electric propulsion: mission characterization and design analysis," *Journal of Electric Propulsion*, vol. 1, no. 1, p. 12, 2022. 6

[6] T. S. Kelso, "Celestrak," https://celestrak.org/, 2023, [Accessed 09-09-2023]. xv, 7, 42

[7] D. A. Vallado and D. Finkleman, "A critical assessment of satellite drag and atmospheric density modeling," *Acta Astronautica*, vol. 95, pp. 141–165, 2014. 7

[8] V. U. Nwankwo, S. K. Chakrabarti, and R. S. Weigel, "Effects of plasma drag on low earth orbiting satellites due to solar forcing induced perturbations and heating," *Advances in Space Research*, vol. 56, no. 1, pp. 47–56, 2015. 8

[9] D. M. Prieto, B. P. Graziano, and P. C. Roberts, "Spacecraft drag modelling," *Progress in Aerospace Sciences*, vol. 64, pp. 56–65, 2014. 8, 9, 10

[10] S. Livadiotti, N. H. Crisp, P. C. Roberts, S. D. Worrall, V. T. Oiko, S. Edmondson, S. J. Haigh, C. Huyton, K. L. Smith, L. A. Sinpetru *et al.*, "A review of gas-surface interaction models for orbital aerodynamics applications," *Progress in Aerospace Sciences*, vol. 119, p. 100675, 2020. 8

[11] P. Maier, J. Skalden, K. Papavramidis, M. Fugmann, S. Klinkner, S. Fasoulas, G. Herdrich, S. Weikert, J. Sanguesa, S. Schäff, A. Wiegand, L. Walpot, B. Duesmann, and

G. Ortega, “System study of a vleo satellite platform applied with the electrodeless irs ipt system,” 05 2022. 8

[12] M. Tisaev, E. Ferrato, V. Giannetti, C. Paissoni, N. Baresi, A. L. Fabris, and T. Andreussi, “Air-breathing electric propulsion: Flight envelope identification and development of control for long-term orbital stability,” *Acta Astronautica*, vol. 191, pp. 374–393, 2022. xv, 9, 11, 18, 21, 23, 27, 44

[13] S. Livadiotti, N. H. Crisp, P. C. Roberts, S. D. Worrall, V. T. Oiko, S. Edmondson, S. J. Haigh, C. Huyton, K. L. Smith, L. A. Sinpetru *et al.*, “A review of gas-surface interaction models for orbital aerodynamics applications,” *Progress in Aerospace Sciences*, vol. 119, p. 100675, 2020. xv, 10

[14] A. Filatyev, A. Golikov, A. Erofeev, S. Khartov, A. Lovtsov, D. Padalitsa, V. Skvortsov, and O. Yanova, “Research and development of aerospace vehicles with air breathing electric propulsion: Yesterday, today, and tomorrow,” *Progress in Aerospace Sciences*, vol. 136, p. 100877, 2023. 10, 15, 16, 17, 18, 23, 26, 27

[15] M. A. M. Serrano, D. Kuijper, J. Sánchez, P. Ramos-Bosch, and D. Sieg, “Goce flight dynamics support to the low orbit and deorbiting operations,” in *International Symposium on Space Flight Dynamics*, 2014. 10

[16] F. Romano, *RF Helicon Plasma Thruster for an Atmosphere-Breathing Electric Propulsion System (ABEP)*, 01 2022. 10, 21

[17] E. Odriozola Olavarría, “Atmospheric models evaluation for space applications,” B.S. thesis, 2018. 11, 50

[18] D. O’Reilly, G. Herdrich, and D. F. Kavanagh, “Electric propulsion methods for small satellites: A review,” *Aerospace*, vol. 8, no. 1, p. 22, 2021. 13, 16, 17

[19] P. Zheng, J. Wu, Y. Zhang, and B. Wu, “A comprehensive review of atmosphere-breathing electric propulsion systems,” *International Journal of Aerospace Engineering*, vol. 2020, pp. 1–21, 2020. xvii, 14, 17, 20, 22, 26

[20] N. H. Crisp, A. M. Rojas, P. C. Roberts, S. Edmondson, S. J. Haigh, B. E. Holmes, V. T. Oiko, L. A. Sinpetru, K. L. Smith, A. Arcos *et al.*, “Experimental results from the satellite for orbital aerodynamics research (soar) mission,” in *Proceedings of the 73rd International Astronautical Congress (IAC), Paris, France*, 2022, pp. 18–22. xv, 15

[21] ESA, "Types of orbits," https://www.esa.int/Enabling_Support/Space_Transportation/Types_of_orbits, 2020, [Accessed 09-09-2023]. xv, 15, 27

[22] JAXA, "Super low altitude test satellite (slats) tsubame has set a guinness world records(r)," https://global.jaxa.jp/press/2019/12/20191224a.html, 2023, [Accessed 09-09-2023]. xv, 15

[23] D. M. Goebel and I. Katz, *Fundamentals of electric propulsion: ion and Hall thrusters*. John Wiley & Sons, 2008. 16

[24] S. Vaidya, C. Traub, F. Romano, G. Herdrich, Y.-A. Chan, S. Fasoulas, P. Roberts, N. Crisp, S. Edmondson, S. Haigh *et al.*, "Development and analysis of novel mission scenarios based on atmosphere-breathing electric propulsion (abep)," *CEAS Space Journal*, vol. 14, no. 4, pp. 689–706, 2022. 16, 17, 22

[25] S. Bathgate, M. Bilek, and D. Mckenzie, "Electrodeless plasma thrusters for spacecraft: a review," *Plasma Science and Technology*, vol. 19, no. 8, p. 083001, 2017. 17

[26] T. Andreussi, E. Ferrato, C. Paissoni, A. Kitaeva, V. Giannetti, A. Piragino, S. Schäff, K. Katsonis, C. Berenguer, Z. Kovacova *et al.*, "The aether project: development of air-breathing electric propulsion for vleo missions," *CEAS Space Journal*, vol. 14, no. 4, pp. 717–740, 2022. 18

[27] K. Nishiyama, "Air breathing ion engine," in *Proc. of 24th International Symposium on Space Technology and Science, Miyazaki, Japan, 2004*, 2004. xvii, 19, 20, 22

[28] J. Ashkenazy, G. Appelbaum, T. Ram-Cohen, A. Warshavsky, I. Tidhar, and L. Rabinovich, "Venμs technological payload-the israeli hall effect thruster electric propulsion system," in *47th Israel Annual Conf. on Aerospace Sciences, Tel-Aviv & Haifa, Israel*, 2007. xv, 20

[29] W. contributors, "Gridded ion thruster," https://en.wikipedia.org/wiki/Talk:Gridded_ion_thruster, 2023, [Accessed 09-09-2023]. xv, 20

[30] D. Di Cara, J. G. Del Amo, A. Santovincenzo, B. C. Dominguez, M. Arcioni, A. Caldwell, and I. Roma, "Ram electric propulsion for low earth orbit operation: an esa study," in *30th International Electric Propulsion Conference*, 2007. 21, 22

[31] G. Cifali, T. Misuri, P. Rossetti, M. Andrenucci, D. Valentian, D. Feili, and B. Lotz, "Experimental characterization of het and rit with atmospheric propellants," in *32nd International Electric Propulsion Conference*, no. 11-15, 2011. 21

[32] V. Hruby, B. Pote, L. Olsen, J. Szabo, P. Rostler, and K. Hohman, “Atmospheric breathing electric thruster for planetary exploration,” 2012. 21, 22

[33] T. Andreussi, G. Cifali, V. Giannetti, A. Piragino, E. Ferrato, A. Rossodivita, M. Andrenucci, J. Longo, and L. Walpot, “Development and experimental validation of a hall effect thruster ram-ep concept,” in *35th International Electric Propulsion Conference*, 2017, pp. 8–12. 22

[34] S. W. Paek, S. Kim, L. Kronig, and O. de Weck, “Sun-synchronous repeat ground tracks and other useful orbits for future space missions,” *The Aeronautical Journal*, vol. 124, no. 1276, pp. 917–939, 2020. xv, 28

[35] R. Birkeland, “On the use of micro satellites as communication nodes - in an arctic sensor network,” Ph.D. dissertation, 02 2019. xv, 28

[36] F. Ricardo, “Low earth orbit nano satellite electrical power system design,” *Instituto Superior Tecnico, Lisboa, Portugal*, 2014. 29

[37] H. D. Curtis, *Orbital mechanics for engineering students.* Butterworth-Heinemann, 2013. 29

[38] V. Janssen, “Understanding coordinate reference systems, datums and transformations,” 2009. 30, 31

[39] ESA, “The earth’s gravity field (geoid),” https://www.esa.int/ESA_Multimedia/Images/2005/04/The_Earth_s_gravity_field_geoid, 2014, [Accessed 09-09-2023]. xv, 30

[40] L. Cazabal-Valencia, S.-O. Caballero-Morales, and J.-L. Martínez-Flores, “Logistic model for the facility location problem on ellipsoids,” *International Journal of Engineering Business Management*, vol. 8, p. 1847979016668979, 2016. [Online]. Available: https://doi.org/10.1177/1847979016668979 xv, 30

[41] MeTatweak, “Theory,” https://coordinates.metatweak.com/theory, [Accessed 09-09-2023]. xv, 30

[42] R. J. Boain, “Ab-cs of sun-synchronous orbit mission design,” 2004. 32

[43] T. M. Inc., “Orbit propagator,” Natick, Massachusetts, United States, 2023. [Online]. Available: https://www.mathworks.com/help/aeroblks/orbitpropagator.html 36

[44] T. M. Inc., “Solver,” Natick, Massachusetts, United States, 2023. [Online]. Available: https://www.mathworks.com/help/simulink/gui/solver.html 37

[45] T. M. Inc., “ecef2lla,” Natick, Massachusetts, United States, 2023. [Online]. Available: https://www.mathworks.com/help/aerotbx/ug/ecef2lla.html 40

[46] T. M. Inc., “atmosnrlmsise00,” Natick, Massachusetts, United States, 2023. [Online]. Available: https://www.mathworks.com/help/aerotbx/ug/atmosnrlmsise00.html 42

[47] T. M. Inc., “fluxsolarandgeomagnetic,” Natick, Massachusetts, United States, 2023. [Online]. Available: https://www.mathworks.com/help/aerotbx/ug/fluxsolarandgeomagnetic.html 42

[48] T. M. Inc., “aeroreadspaceweatherdata,” Natick, Massachusetts, United States, 2023. [Online]. Available: https://www.mathworks.com/help/aerotbx/ug/aeroreadspaceweatherdata.html 42

[49] N. Wallace, P. Jameson, C. Saunders, M. Fehringer, C. Edwards, and R. Floberghagen, “The goce ion propulsion assembly–lessons learnt from the first 22 months of flight operations,” in *32nd International Electric Propulsion Conference*, no. 11-15, 2011. xvi, 47, 48, 49

[50] ESA, “Goce (gravity field and steady-state ocean circulation explorer),” https://www.eoportal.org/satellite-missions/goce#spacecraft, 2012, [Accessed 09-09-2023]. 47

[51] ESA, “Facts and figures,” https://www.esa.int/Applications/Observing_the_Earth/FutureEO/GOCE/Facts_and_figures, [Accessed 25-07-2023]. 47

[52] ThrustMe, “The npt30-i2,” https://www.thrustme.fr/products/npt30-i2, [Accessed 09-09-2023]. 58

[53] Exotrail, “Exomg - nano thruster performs beyond expectations,” https://www.exotrail.com/blog/exomg-tm-nano-thruster-performs-beyond-expectations, 2019, [Accessed 09-09-2023]. 58